Cover Letter

Cube2sph: A Toolkit Enabling Flexible and Accurate Continental-scale Seismic Wave Simulations using the SPECFEM3D_Cartesian Package

Tianshi Liu,Kai Wang,Yujiang Xie,Bin He,Ting Lei,Nanqiao Du,Ping Tong,Yingjie Yang,Catherine A. Rychert,Nicholas Harmon,Giovanni Grasselli,Qinya Liu

Dear Editors-in-Chief,

Please find the enclosed manuscript "Cube2sph: A Toolkit Enabling Flexible and Accurate Continental-scale Seismic Wave Simulations using the SPECFEM3D Package" which we are submitting for exclusive consideration for publication in Computers & Geosciences. We confirm that the submission follows all the requirements and includes all the items of the submission checklist.

The manuscript presents a toolkit, Cube2sph, to aid flexible mesh generation and accurate seismic wave simulations at continental scales ($10 - 60°$) using the open-source community-based SPECFEM3D package. The toolkit mainly addresses two difficulties in continental-scale seismic wave simulations: (1) accurate incorporation of the Earth's spherical curvature and (2) implementation of perfectly matched layer (PML) on deformed meshes to effectively reduce artificial reflections. Along with a description of this toolkit, a series of numerical examples are presented in this manuscript to illustrate its effectiveness in accurately taking into account the Earth's spherical curvature and improving the accuracy with the use of PML.

We provide the source codes in a public repository with details listed in the section "Code availability".

Thanks for your consideration.

Sincerely,

Tianshi Liu, Kai Wang, Yujiang Xie, Bin He, Ting Lei, Nanqiao Du, Ping Tong, Yingjie Yang, Catherine A. Rychert, Nicholas Harmon, Giovanni Grasselli, Qinya Liu
Corresponding author: Tianshi Liu
Department of Earth Sciences, University of Toronto, Toronto, Ontario, Canada, tianshi.liu@mail.utoronto.ca

Highlights

`Cube2sph`: A Toolkit Enabling Flexible and Accurate Continental-scale Seismic Wave Simulations using the `SPECFEM3D_Cartesian` Package

Tianshi Liu,Kai Wang,Yujiang Xie,Bin He,Ting Lei,Nanqiao Du,Ping Tong,Yingjie Yang,Catherine A. Rychert,Nicholas Harmon,Giovanni Grasselli,Qinya Liu

- Flexible mesh generation for continental-scale seismic wave simulations with spherical geometry accurately incorporated in the open-source community-based `SPECFEM3D_Cartesian` package.
- Perfectly matched layer is implemented on curvilinear grids to accommodate the deformed mesh.
- Numerical examples show the effectiveness of this toolkit and provide practical guidance to applications in continental-scale seismic wave simulations.

Cube2sph: A Toolkit Enabling Flexible and Accurate Continental-scale Seismic Wave Simulations using the SPECFEM3D_Cartesian Package

Tianshi Liu[a], Kai Wang[b], Yujiang Xie[c], Bin He[i,j], Ting Lei[a], Nanqiao Du[a], Ping Tong[d,e,f], Yingjie Yang[g], Catherine A. Rychert[c,k], Nicholas Harmon[c,k], Giovanni Grasselli[h] and Qinya Liu[a,i]

[a]*Department of Earth Sciences, University of Toronto, Toronto, Ontario, Canada*
[b]*School of Earth and Space Sciences, University of Science and Technology of China, Hefei, Anhui, China*
[c]*University of Southampton, Ocean and Earth Science, Southampton, UK*
[d]*Division of Mathematical Sciences, School of Physical and Mathematical Sciences, Nanyang Technological University, 637371, Singapore*
[e]*Earth Observatory of Singapore, Nanyang Technological University, 639798, Singapore*
[f]*Asian School of the Environment, Nanyang Technological University, 639798, Singapore*
[g]*Department of Earth and Space Sciences, Southern University of Science and Technology, Shenzhen, Guangdong, 518055, China*
[h]*Department of Civil & Mineral Engineering, University of Toronto, Toronto, Ontario, Canada*
[i]*Department of Physics, University of Toronto, Toronto, Ontario, Canada*
[j]*Department of Geosciences, the University of Texas at Dallas, Richardson, TX 75080, USA*
[k]*Woods Hole Oceanographic Institution, Woods Hole, MA, USA*

ARTICLE INFO

Keywords:
Seismology
High-performance computing
Spectral-element method
Perfectly matched layer

ABSTRACT

To enable flexible and accurate seismic wave simulations at continental scales ($10° - 60°$) based on the spectral-element method using the open-source `SPECFEM3D_Cartesian` package, we develop a toolkit, `Cube2sph`, that allows the generation of customized spherical meshes that account for the Earth's curvature. This toolkit enables the usage of the perfectly matched layer (PML) absorbing boundary condition even when the artificial boundaries do not align with the coordinate axes. A series of numerical experiments are presented to validate the effectiveness of this toolkit. From these numerical experiments, we conclude that (1) continental-scale seismic wave simulations, especially surface wave simulations, can be more efficiently performed without the loss of accuracy by truncating the mesh at an appropriate depth, (2) curvilinear-grid PML can be used to effectively suppress artificial reflections for seismic wave simulations at continental scales, and (3) the Earth's spherical geometry needs be accurately meshed in order to obtain accurate simulation results for study regions larger than 8°.

CRediT authorship contribution statement

Tianshi Liu: Writing the computer programs, writing the manuscript. **Kai Wang:** Establishing the framework of the project, refining the manuscript. **Yujiang Xie:** Establishing the framework of the project, refining the manuscript. **Bin He:** Establishing the framework of the project, refining the manuscript. **Ting Lei:** Co-writing the computer programs, refining the manuscript. **Nanqiao Du:** Co-writing the computer programs, refining the manuscript. **Ping Tong:** Establishing the framework of the project, refining the manuscript. **Yingjie Yang:** Supervising the project, refining the manuscript. **Catherine A. Rychert:** Supervising the project, refining the manuscript. **Nicholas Harmon:** Supervising the project, refining the manuscript. **Giovanni Grasselli:** Supervising the project, refining the manuscript. **Qinya Liu:** Supervising the project, establishing the framework of the project, discussions on program structure, refining the manuscript.

ORCID(s):

1. Introduction

Numerical simulation of seismic waves is key to seismic hazard assessment (e.g., Graves, 1998; Pitarka, 1999; Zhao et al., 2007) as well as full-waveform source (e.g., Liu et al., 2004; Wang and Zhan, 2020) and structural (e.g., Tape et al., 2010; Fichtner et al., 2010; Zhu et al., 2015; Wang et al., 2019) inversion. With the development of numerical algorithms and high-performance computation facilities, several numerical packages have been developed to perform seismic wave simulations in 3-D heterogeneous Earth models, particularly during the last two decades, e.g., `SPECFEM` (Komatitsch and Tromp, 1999; Komatitsch et al., 2004), `SES3D` (Gokhberg and Fichtner, 2016), `RegSEM` (Cupillard et al., 2012) and `SeisSol` (Dumbser and Käser, 2006).

In particular, the open-source community-based `SPECFEM3D_Cartesian` (https://github.com/geodynamics/specfem3d) and `SPECFEM3D_GLOBE` (https://github.com/geodynamics/specfem3d_globe) packages have been developed based on the spectral element method (SEM) (Komatitsch and Tromp, 2002a,b; Komatitsch et al., 2004) to simulate seismic waves in 3-D Earth models at local, regional and global scales. In principle, the `SPECFEM3D_Cartesian` package can solve the seismic-wave equation in a computation domain with any geometry. However, its internal mesher can only produce cube-shaped meshes. When the Earth's spherical geometry needs to be accounted for, the Universal Transverse Mercator projection (UTM, Snyder, 1982) is used to map geographic coordinates to Cartesian coordinates, which may not be accurate enough for regions much larger than a UTM zone ($\sim 6°$). Therefore, the current `SPECFEM3D_Cartesian` package is most commonly used for wave simulations at local ($< 2°$) and regional ($2° - 10°$) scales. Despite this limitation, the `SPECFEM3D_Cartesian` package aims to support complexity and flexibility for wave simulations. Both its internal mesher and external meshing tools such as `GEOCUBIT` (Casarotti et al., 2008) support customized surface and interface topography, user-provided tomographic models, and user-defined mesh refinements. On the other hand, the mesher in the `SPECFEM3D_GLOBE` package uses the "cubed sphere" mapping (Ronchi et al., 1996; Komatitsch and Tromp, 2002a) to accurately incorporate the Earth's spherical geometry, and can mesh the entire globe into six "chunks" to conduct global wave simulations. Continental-scale (10°-60°) simulations, which require accurate honouring of the Earth's spherical curvature, have often been carried out using one chunk of the global mesh in the past (e.g., Zhu et al., 2015; Chen et al., 2015; Tao et al., 2018). Although the one-chunk mesh can provide accurate continental-scale simulations, the mesh goes down to a depth inside the inner core, resulting in a waste of computational resources for applications when deep structures are irrelevant (e.g., surface-wave or ambient-noise tomography and seismic hazard assessment). The Cartesian Meshing Spherical Earth (CMSE) package (Li et al., 2022) generates a depth-truncated spherical mesh by treating the Earth's curvature as topography and simulates seismic waves using `SPECFEM3D_Cartesian`. Despite its success on domains with a spatial scale of $\sim 12°$, the distortion is too large to guarantee good enough mesh quality for numerical simulations on larger domains. The recent development of the `SPECFEM3D_GLOBE` package (as of April 1, 2022) allows the mesh to be truncated at several fixed depths, but no published study has been conducted to show the effect of truncation on simulation results in detail. In addition, only a limited number of choices for interface topography are offered in the package, the positions of mesh doubling layers are hard-coded, and the mesh can only be partitioned in a fixed way. In other words, although it is possible to use the `SPECFEM3D_GLOBE` package at a wide range of scales, it is designed and optimized specifically for global-scale simulations.

Another challenge for continental-scale wave simulations is implementing absorbing boundaries at the sides and the bottom of the computation domain to suppress artificial reflections. The waves reflected from an artificial boundary can contaminate the main signal when the source and receiver are close to that boundary. The Stacey boundary condition (Clayton and Engquist, 1977) has been used widely in full wave simulations to reduce the amplitude of artificial reflections with no additional computational cost, but it becomes ineffective when the incident angle is close to 90°. The perfectly matched layer (PML, Bérenger, 1999; Komatitsch and Martin, 2007), on the other hand, despite the additional computational cost, can effectively absorb the outgoing waves even at grazing incidence. The PML implementation in the current `SPECFEM3D_Cartesian` package (Wang et al., 2004; Xie et al., 2014) assumes that the artificial boundaries align with the coordinate axes, which is no longer valid for continental-scale simulations when the meshes must be deformed to accommodate the spherical geometry of the Earth. In the current `SPECFEM3D_GLOBE` package, no PML implementation is provided, and only the Stacey boundary condition or a sponge layer can be used to absorb the artificial reflections.

To simultaneously address these two difficulties in continental-scale seismic wave simulations – accurately incorporating the spherical geometry and effectively suppressing the artificial reflections, we develop a toolkit, `Cube2sph`, that allows for flexible and accurate continental-scale wave simulations using the `SPECFEM3D_Cartesian` package. The toolkit creates a hexahedral mesh that honors the Earth's spherical curvature by applying the "cubed sphere" transformation to a cube-shaped mesh generated by the `SPECFEM3D_Cartesian` internal mesher or an external meshing tool such as `GEOCUBIT` (Casarotti et al., 2008). It also provides an implementation of curvilinear-grid PML based on auxiliary differential equations (ADE) in the `SPECFEM3D_Cartesian` package. With this toolkit, continental-scale seismic wave simulations can be carried out using the `SPECFEM3D_Cartesian` package with accuracy and flexibility.

The remaining sections of this article are organized as follows: in Section 2, the approach to generate a mesh with spherical geometry and to implement curvilinear-grid PML is described; in Section 3 we illustrate the workflow of the `Cube2sph` toolkit and highlight its flexibility in mesh generation through an example incorporating surface and interface topography and 3-D heterogeneous tomographic model; in Section 4, we demonstrate the effectiveness of our toolkit in performing continental-scale simulations with numerical experiments.

2. Methods

2.1. Discretizing a slice of the Earth using the "cubed sphere" transformation

We first describe how to construct the mesh for a computation domain with the Earth's spherical curvature incorporated (which we refer to as a *spherical computation domain* throughout this article) using the `Cube2sph` toolkit. Here a computation domain refers to a 3-D volume on which the seismic-wave equations are numerically solved, and a mesh on the computation domain refers to a subdivision of the computation domain into non-overlapping elements. The mesh used for 3-D SEM computation is composed of hexahedral elements, i.e., each element is a deformed cube with 8 vertices, 12 edges and 6 faces. The geometry of each element in the mesh is defined by the coordinates of its anchor points from which the edges, faces and volume within the element are then defined through interpolation (Komatitsch and Tromp, 1999; Tromp et al., 2008). Most common hexahedral 3-D elements used in SEM have either $2^3 = 8$ (denoted as *HEX8*, 8 vertices) or $3^3 = 27$ (denoted as *HEX27*, 8 vertices + 12 edge centers + 6 face centers + 1 volume center) anchor points. We use HEX27 elements to better accommodate curved edges and non-planar faces for the simulations in this study, in alignment with the implementation in `SPECFEM3D_GLOBE`. Since we focus on spherical computation domains, throughout this article, wherever angle is used to describe distance, it should be understood as great-circle distance.

It is generally straightforward to construct a mesh on a cube-shaped domain. For example, regular mesh with doubling in depth can be created by the `meshfem3D` module in the `SPECFEM3D_Cartesian` package or external meshing tools such as `GEOCUBIT`. By applying an appropriate transformation to all the anchor points of a cube-shaped mesh, a mesh on the spherical computational domain can be obtained.

The "cubed sphere" transformation (Ronchi et al., 1996; Komatitsch and Tromp, 2002a) is commonly used to map a cube-shaped domain into a domain with the spherical curvature. Let us suppose that the horizontal size of the spherical computation domain is $X \times Y$ (represented as radians), and the maximum depth is D (Figure 1a). We can first construct a mesh on a cube-shaped domain $[-\frac{RX}{2}, \frac{RX}{2}] \times [-\frac{RY}{2}, \frac{RY}{2}] \times [-D, 0]$ as in Figure 1(b), where R is the radius of the Earth, and then apply the "cubed sphere" transformation to the anchor points of the cube-shaped mesh to obtain a mesh on the spherical computation domain (Figure 1c). Specifically, it maps a point (ξ, η, ζ) in the cube-shaped domain (Figure 1b) to a new point (x, y, z) in the spherical domain (Figure 1c) based upon

$$
\begin{aligned}
z &= \frac{(R+\zeta)}{\sqrt{1+\tan^2\frac{\xi}{R}+\tan^2\frac{\eta}{R}}},\\
x &= -z\tan\frac{\eta}{R},\\
y &= z\tan\frac{\xi}{R},
\end{aligned}
\tag{1}
$$

similar to the mapping of *chunk AB* in Komatitsch and Tromp (2002a). The effect of the transformation is illustrated in Figure S1. Clearly, by design,

$$x^2 + y^2 + z^2 = (R + \zeta)^2, \tag{2}$$

which implies that the "cubed sphere" transformation maps a horizontal plane in the cube-shaped mesh into a spherical surface with a constant radius, and a point at a specific depth in the cube-shaped mesh will be mapped to a point at the same depth in the spherical mesh. Using this property, surface and interface topography can be built into the cube-shaped mesh, and the "cubed sphere" transformation will map the free surface and the interfaces to correct depths. Similarly, tomographic models can be defined in the cube-shaped mesh, and each point in the spherical mesh will take the corresponding structural properties before the "cubed sphere" transformation.

After the "cubed sphere" transformation, the spherical domain is always centered at the North Pole, with one side perpendicular to the prime meridian (Figure S1). A subsequent coordinate transformation can move its center to a desired location and rotate to a desired orientation.

The mesh generated by the `Cube2sph` toolkit accurately honors the Earth's spherical curvature and is therefore suitable for continental-scale wave modelings, in which the computation domain is so large that the curvature must be accurately considered. Moreover, in combination with the `meshfem3D` module in the `SPECFEM3D_Cartesian` package, the `Cube2sph` toolkit allows for customized vertical layering: doubling layers can be placed at any desired depth, surface and interface topography can be incorporated and the computation domain can be truncated at any depth. If an external mesher such as `GEOCUBIT` is used to produce the cube-shaped mesh, interface topography can be honored and mesh refinement can be achieved more flexibly. Although the `SPECFEM3D_GLOBE` mesh is also produced using the "cubed sphere" transformation to take into account the Earth's spherical geometry and can also be truncated at certain depths, only a few truncation depths are allowed. Moreover, the `SPECFEM3D_GLOBE` package does not allow users to freely choose interface topography, the positions of doubling layers and the way the mesh is partitioned. However, these features are often desired for continental-scale wave simulations. Therefore, the `Cube2sph` toolkit complements the `SPECFEM3D_GLOBE` package and allows for more flexibility in continental-scale wave simulations.

2.2. Implementing perfectly matched layer (PML) on curvilinear grids

In order to effectively absorb the outgoing waves with grazing incidence, the PML boundary condition was developed first for electromagnetic equations (Bérenger, 1999), and was applied to elastodynamic modeling with split-field implementations (e.g., Komatitsch and Tromp, 2003), convolutions (e.g., Komatitsch and Martin, 2007; Martin et al., 2008; Martin and Komatitsch, 2009; Xie et al., 2014) and auxiliary differential equations (ADE-PML, e.g., Martin et al., 2010; Zhang and Shen, 2010). The PML implements a layer with finite thickness outside the physical computational domain and imposes attenuation on the waves inside this layer. Although additional computational cost is required, the outgoing waves can be accurately suppressed even in the grazing incidence case.

The formulas for the PML are often derived with the assumption that the boundaries align with the coordinate axis, as is the case in the current implementation of PML in the `SPECFEM3D_Cartesian` package (Wang et al., 2004; Xie et al., 2014). However, in continental-scale simulations, such a restriction sometimes cannot be satisfied because of the need to honor the Earth's spherical curvature. Early efforts have been made to implement PML in cylindrical or spherical coordinates (e.g., Collino and Monk, 1998; Liu, 1999) or orthogonal curvilinear coordinates (e.g., Festa and Vilotte, 2005). Gao and Zhang (2008) and Zhang and Gao (2011) developed PML in arbitrary curvilinear grids based on split-field implementations in tetrahedral elements. Zhang et al. (2014) adopted a similar approach to develop curvilinear ADE-PML for finite-difference elastodynamic simulations using local coordinate transformation, and also found that the multi-axial PML (MPML, Meza-Fajardo and Papageorgiou, 2008) can help avoid instability.

To implement PML on (possibly non-orthogonal) curvilinear grids in the `SPECFEM3D_Cartesian` package, we incorporate a coordinate transformation in the formulation of ADE-PML (Martin et al., 2010), which is equivalent to the treatment of Zhang et al. (2014), and derive the weak form of the momentum equation and its auxiliary differential equation to fit into the SEM framework. The detailed derivation can be found in Appendix A.

3. Workflow of the `Cube2sph` toolkit and an example of mesh generation

In this section, we briefly describe the steps to build a mesh and perform seismic wave simulations using the `Cube2sph` toolkit, illustrated through a mesh example that incorporates customized surface and interface topography, ellipticity, doubling layers, and tomographic structural models. Theses steps are summarized in the flowchart shown in Figure 2.

3.1. Setting up mesh parameters and building a cube-shaped mesh

The first step of building a mesh is to set the mesh parameters in the parameter files, e.g., mesh size, number of elements, truncation depth, vertical layering, doubling layers and PML layers. As an example, we build a $22° \times 22°$, 770 km-thick mesh for the region of Alaska (Figure 3), with PML layers of 8-element thick on the sides and 2-element thick at the bottom. To accommodate vertical velocity changes from the sediment ($V_S \approx 1.5 - 2.8$ km/s) to the crust ($V_S \approx 2.8 - 4.2$ km/s), and then to the mantle ($V_S \approx 4.2 - 5$ km/s), we use two doubling layers, one in the crust and one beneath Moho. The mesh has 400×400 elements in the top layer.

The next step is to prepare the input tomographic model files. In this example, we aim to honor sedimentary basins at depths between $4-8$ km, and the Moho between $12-16$ km beneath the ocean and $25-45$ km beneath the continent. At other depths, the interfaces run through elements and are not honored, similar to the current implementation of the

SPECFEM3D_GLOBE package, as documented in Tromp et al. (2010). Such treatment is necessary to avoid severe deformation of the elements when using the internal mesher, because it cannot handle complex geometry very well. If an external meshing tool such as GEOCUBIT is used, this limitation can be remedied. The depths of the sedimentary basins and Moho are defined by extracting the surfaces of $V_S = 2.8\,\mathrm{km/s}$ and $V_S = 4.2\,\mathrm{km/s}$ from a shear-velocity model obtained by Berg et al. (2020). In regions that are not covered by the Berg et al. (2020) model, the interfaces are extracted from Crust 1.0 (Laske et al., 2013). A tomographic model is generated by merging the global crustal model Crust 1.0, a regional shear-velocity model by Berg et al. (2020) and the global mantle model S40RTS (Ritsema et al., 2011), and is interpolated onto the grid points of the mesher. Note that the anchor points of the cube-shaped mesh, the interfaces and the tomographic model are all represented in Cartesian (ξ, η, ζ) coordinates.

After mesh parameters are set and model files are prepared, the cube-shaped mesh can be generated. For simplicity, the cube-shaped mesh in this study is built using the internal mesher of the SPECFEM3D_Cartesian package. More complex cube-shaped meshes can also be built with external meshers such as GEOCUBIT. The cube-shaped mesh is then partitioned to enable parallel computing using SCOTCH.

3.2. Applying the “cubed sphere” transformation

Before applying the “cubed sphere” transformation, the xgenerate_databases program needs to be executed on the cube-shaped mesh to setup the numbering and PML damping parameters. After that, the "cubed sphere" transformation (eqn. 1) is applied to create the spherical geometry. As mentioned in Section 2.1, the mesh can be further moved and rotated to cover the region of interest. In this example, the mesh is moved such that its center is $(62.5°\ N, 151.0°\ W)$, and is rotated 20° counter-clockwise, so that it covers the entire region of Alaska. The nodes of the mesh are then stretched vertically to honor the Earth’s ellipticity. Finally, the xgenerate_databases program needs to be executed again on the spherical mesh to setup the database for the solver. Figure 3 shows the final mesh with surface and Moho topography and the assigned shear velocity that can provide accurate simulation for periods longer than 9 s.

3.3. Performing forward simulation

In the SPECFEM3D_GLOBE package, the source and receivers are listed in a FORCESOLUTION file (or a CMTSOLUTION file if the source is a double couple) and a STATIONS file, in which the locations are given in geographic coordinates, i.e., latitude, longitude and depth. When using the SPECFEM3D_Cartesian package with the Cube2sph toolkit, similar files need to be prepared, but locations must be given in Cartesian coordinates. We provide programs to convert source and station files from the SPECFEM3D_GLOBE format to the SPECFEM3D_Cartesian format. After coordinate conversion, the SPECFEM solver can be launched to carry out the forward simulation. The computed seismograms are directly written in Cartesian (x, y, z) coordinates. However, the seismograms are most commonly used in the easting, northing and vertical components, i.e., in the local (E, N, Z) coordinates (easting, northing, vertical). To deal with the coordinate transformation, we provide a script in the `Cube2sph` toolkit to rotate the seismograms (and the adjoint sources when performing adjoint simulations) between the two coordinate systems.

4. Numerical experiments

4.1. Comparison with the `SPECFEM3D_GLOBE` one-chunk mesh

In this section, we present numerical experiments on a horizontally $20° \times 20°$ computation domain and compare the simulation results from the `Cube2sph` mesh with those based on the `SPECFEM3D_GLOBE` one-chunk mesh to examine the effect of depth truncation. As discussed in Section 2.1, the `Cube2sph` mesh (Figure 1c) is constructed by first generating a cube-shaped mesh using the `SPECFEM3D_Cartesian` internal mesher and then applying the "cubed sphere" transformation as in eq. (1), and in this experiment it extends from the Earth's surface down to 220 km. On the other hand, the one-chunk mesh (Figure 1a) is constructed directly using the `SPECFEM3D_GLOBE` internal mesher. The `Cube2sph` mesh is identical to the upper part of the one-chunk mesh (outlined by the green dashed line in Figure 1a), with both meshes consisting of 320×320 elements horizontally at the top, and 4 layers in the crust above the Moho at 24.4 km depth, 4 layers in mantle between $24.4 - 80$ km depth, and 10 layers between $80 - 220$ km depth. A doubling layer is implemented immediately beneath the Moho in both meshes to adjust the element size based the vertical velocity change. The one-chunk mesh extends down to 5420 km depth, beneath the inner-core boundary, and has two additional doubling layers at 1650 km and 3860 km depth. To simplify the numerical experiments, topography and ellipticity are neglected, and the 1-D isotropic PREM model (Dziewonski and Anderson, 1981) with the one-layer crust is used. Both meshes can provide accurate simulations for waves of 5 s period and above. The Stacey absorbing condition is implemented at all artificial boundaries.

We carry out forward simulations with the `Cube2sph` mesh and the one-chunk mesh, using the `SPECFEM3D_Cartesian` solver and the `SPECFEM3D_GLOBE` solver respectively, and compare the computation time and synthetic waveforms. For comparison purpose, we use a same time step of 0.025 s for both simulations, which satisfies the CFL stability condition (Courant et al., 1928) for both meshes. We run the time iteration for $35,800$ steps to generate 15-minute long waveforms. As shown in Figure 1c, we place a vertical vector point force (yellow star) on the free surface near one corner of the mesh, 2° away from both sides. Four receivers (green triangles) are placed on the free surface, 2° away from one of the sides, and at a great-circle distance of 4°, 8°, 12° and 16° from the source, respectively. The source time function is a Ricker wavelet with a dominant period of 5 s. All synthetic waveforms are filtered between $6 - 50$ s to exclude the high-frequency numerical noise, as shown in Figures 4. The simulations are performed on 400 2.4-GHz CPU cores in parallel on the Niagara cluster at the SciNet HPC Consortium (Ponce et al., 2019). Table 1 outlines the number of elements and Gauss-Lobatto-Legendre (GLL) points in the two meshes. By truncating at 220 km, the

Table 1
Number of elements and number of GLL points of the one-chunk mesh and the `Cube2sph` mesh used for the simulations as shown in Figure 1, as detailed in Section 4.1

	number of elements	number of GLL points
`one-chunk`	4,780,800	331,127,600
`Cube2sph`	921,600	62,946,773

`Cube2sph` mesh is able to reduce the number of elements by a factor of 5.

Figure 4 compares vertical-component synthetic seismograms (i.e., Z-Z components of the Green's functions) generated at the four receivers using the `Cube2sph` mesh (dashed red lines) and the `SPECFEM3D_GLOBE` one-chunk mesh (blue lines). The global simulation result (green lines) obtained by the `AxiSEM` package (Nissen-Meyer et al., 2014) is also displayed in the background as a reference. The `AxiSEM` package provides accurate whole-Earth wavefield simulations assuming an axisymmetric Earth model, and therefore its results are considered ground truth and are compared with the results of the `Cube2sph` mesh and the `SPECFEM3D_GLOBE` one-chunk mesh to illustrate the effects of depth truncation and imperfect absorbing boundaries. The current `AxiSEM` package approximates the waveform at a receiver with the value at its nearest grid point, resulting in a small time shift. To produce more accurate simulation results, we use a slightly modified version of `AxiSEM` to interpolate the wavefield at the receiver. If we define the *relative waveform difference* between two traces $s_1(t)$ and $s_2(t)$ as

$$\frac{\int |s_1(t) - s_2(t)|^2 \mathrm{d}t}{\sqrt{\int |s_1(t)|^2 \mathrm{d}t}\sqrt{\int |s_2(t)|^2 \mathrm{d}t}}, \tag{3}$$

then it can be observed that waveforms generated with the `SPECFEM3D_GLOBE` one-chunk mesh and the `Cube2sph` mesh are almost identical with the relative waveform difference below 0.5%. As it is known, surface wave signals dominate seismic waveforms. This small relative waveform difference demonstrates that truncating the mesh at 220 km does not substantially affect the surface-wave simulation over the epicentral distance range in this numerical experiment. However, before the onset of the direct surface-wave arrival, discrepancies can be observed in the body-wave phases of the waveforms as seen in Figure 4b, which is a zoom-in of Figure 4a before the direct surface-wave arrival. The issue of body-wave modeling based on the `Cube2sph` toolkit will be further discussed in Section 4.4.

On the other hand, both the `SPECFEM3D_GLOBE` one-chunk waveforms and the `Cube2sph` waveforms are substantially different from the global waveforms by `AxiSEM`, with a relative waveform difference of up to 35% between the results of `Cube2sph` and `AxiSEM`, mainly due to the artificial reflections from domain boundaries on the sides as a result of the insufficient Stacey absorbing boundary condition. By observation and theoretical analysis, we identify three main surface-wave related arrivals in these seismograms (as marked by the shaded areas in Figure 4a): (1) the direct surface-wave arrival from the source to the receiver, (2) the wave reflected off the artificial boundary parallel to

Table 2
Computation time and error using the `Cube2sph` mesh with PML absorbing boundary condition, and the Stacey boundary condition on the original domain as well as the domain enlarged horizontally by factor of 1.2, as discussed in Section 4.2. The error is measured based on the maximum relative waveform difference (eqn. 3) by comparing to the `AxiSEM` results.

	PML	Stacey	Stacey with enlarged domain
computation time (s)	1959.1	1244.1	1789.1
error	0.3%	35.9%	14.0%

the source-receiver line (side A in Figure 1c), and (3) the wave reflected at the artificial boundary perpendicular to the source-receiver line (side B in Figure 1c). Overall, for this numerical setup, at epicentral distance $\geq 8°$, the contamination of the artificial reflections becomes non-negligible, because the arrivals of the artificial reflections overlap with the main phases, and the Stacey boundary condition becomes ineffective for large incident angles. This issue can be addressed by using the PML boundary condition as shown in Section 4.2.

Note that the same mesh as generated by `Cube2sph` (Figure 1c) can be also generated using the `SPECFEM3D_GLOBE` package with the newly added the regional mesh cutoff feature. Based on our numerical experiment, as expected, the simulation results on the `Cube2sph` mesh and the `SPECFEM3D_GLOBE` one-chunk mesh are identical when the truncation depths are the same.

4.2. Comparison between PML and the Stacey absorbing condition

In this section, we present numerical experiments to show the effectiveness of the curvilinear PML boundary implementation for the `SPECFEM3D_Cartesian` mesh. We compare both the computation times and synthetic waveforms between implementations with PML and Stacey boundary conditions. The mesh, source-receiver geometry, source time function, and velocity model are the same as the numerical experiment in Section 4.1. For the mesh with PML boundary, the PML layer is 4 elements thick at all four sides and 2 elements thick at the bottom. To properly balance the different computation load of PML and non-PML elements, we use the `SCOTCH` package (Pellegrini, 2010) to partition the mesh to different processors. An optimal value of 5.5 for the load of PML elements is found heuristically and is used in all numerical experiments.

Figure 5 illustrates the comparison of waveforms generated using the `Cube2sph` mesh with the Stacey boundary condition (blue lines) and with PML (red dashed lines), and the full-globe simulation generated using `AxiSEM` is displayed in the background as reference (green lines). Here we only show the Z-Z component of the Green's function, and the radial-component seismogram due to a force in radial direction (R-R component) and the transverse-component seismogram due to a force in transverse direction (T-T component) are shown in Figures S2 and S3. Table 2 compares the computation time and error of simulations using PML and Stacey boundary conditions. In this example, even though the `Cube2sph` simulation using PML with load balancing takes $\sim 57\%$ more time than that using the Stacey boundary condition, the artificial surface-wave reflections present in the simulation with the Stacey boundary condition are effectively absorbed with the curvilinear PML boundary condition (Figure 5a), leading to a $\leq 0.3\%$ relative waveform difference between the results of `Cube2sph` with PML and `AxiSEM`. However, the body-wave phases still cannot be accurately simulated with PML for epicentral distances beyond 8° due to the bottom truncation of the simulation domain (Figure 5b).

A potential alternative solution to avoid the contamination of artificial reflections with the Stacey boundary condition is to enlarge the computation domain such that the source and receivers are far enough away from the artificial boundaries. Here we enlarge the computation domain horizontally by a factor of 1.2 to $24° \times 24°$ with the same element size, resulting in 384×384 elements at the top layer of the new mesh. All other parameters remain the same as in Section 4.1. Figure 6 shows the waveforms generated in the regular domain using PML (red dashed lines), and in the enlarged computation domain with the Stacey boundary condition (blue lines). Although in the case of the Stacey boundary condition, the contamination by artificial reflections is alleviated by using the enlarged computation domain, it is still clearly visible at 12° and 16°, leading to a $\leq 14\%$ relative waveform difference with the `AxiSEM` results. Table 2 shows that using the Stacey boundary condition in the computation domain enlarged by a factor of 1.2 takes a similar amount of computation time as using PML in the original domain. Therefore, considering the excellent waveform fits to the global reference, we believe PML may be a more effective choice in absorbing artificial reflections than slightly enlarging the computation domain under the Stacey boundary condition.

Note that the comparisons of waveform and computation time may vary for applications with different mesh size, source receiver geometry, and period band of interest. Nevertheless, these numerical experiments show that considering both the effectiveness of absorbing artificial reflections and the computation time, at least in certain cases, using PML with proper load balancing is a better choice than stacy boundry condition with enlarged domain. We suggest that for specific applications with different mesh parameters, numerical tests be performed first to determine the better boundary condition to use in balancing the numerical cost with potential reflections from artificial boundaries.

4.3. Comparison between the “cubed sphere” transformation and the UTM projection

For local- and regional-scale studies, the UTM projection (Snyder, 1982) is frequently used to project a geographical coordinate (Latitude, Longitude) to a local Cartesian coordinate (Easting, Northing). In the UTM system, the Earth is divided into 60 UTM zones, each spanning 6° in longitude. Inside each UTM zone, the distortion of the UTM projection is small. Therefore, for study regions that are small enough to fit inside a UTM zone, waveforms can be relatively accurately simulated on Cartesian meshes after the UTM projection. However, for study regions larger than a UTM zone, the distortion of the UTM projection can be too large to produce accurate enough simulation results. In this section, we compare the waveforms at different epicentral distances obtained using the UTM projection with those using the `Cube2sph` mesh when the Earth’s curvature is fully accounted for.

We use a horizontally $20° \times 20°$ computation domain centered at $(0°, 3° E)$, which is the center of UTM zone 31. We generate a spherical mesh using the `Cube2sph` package, and a Cartesian mesh using the UTM projection at UTM zone 31. The number of elements, vertical layerings and velocity models in both meshes are the same as in Section 4.1. Topography is neglected, but because the UTM projection considers the Earth's ellipticity, we include ellipticity in the `Cube2sph` mesh as well for consistency. To exclude the contamination of artificial reflections, we use PML in both meshes, with the PML layer being 4 elements thick at all four sides and 2 elements thick at the bottom. For the `Cube2sph` mesh, we use the curvilinear-grid PML discussed in Section 2.2, and for the UTM mesh, we use the CPML implemented in the current `SPECFEM3D_Cartesian` package. To keep the discussion simple, we only show the Z-Z component of the Green's functions in this section. Results for R-R and T-T components can be found in Figures S7-S18. Furthermore, we only focus on examining the difference in surface waves here. Since surface waves are accurately simulated using the `Cube2sph` mesh and the PML absorbing boundary condition as shown by the numerical experiment in Section 2.2 and in Figure 5, we treat the results of the `Cube2sph` mesh with PML as references to measure the errors of the UTM results. To investigate the accuracy of the UTM projection for different source-receiver geometry, we conduct numerical experiments with six different source-receiver configurations (Figure 7) with waveforms shown in Figures 8-10 and S4-S6. To the left of the waveforms, we display the values of the relative waveform difference defined by eqn. (3) and the cross-correlation time shift between the `Cube2sph` and the UTM results as two measurements of the discrepancy between two methods.

When the source is at the center of the UTM zone (Figure 7a), the receivers up to 6° longitudinally away from the source have less than 10% relative waveform difference between the two meshes (Figure 8). In contrast, along the meridian (Figure 7b), the relative waveform difference is only 2.54% when the epicentral distance is as large as 8° (Figure S4), indicating the distortion of the UTM projection is smaller along the meridians than along the parallels. When the source is out of the UTM zone and is 5° longitudinally away from the edge of the UTM zone (Figure 7c, d), the discrepancy between UTM and `Cube2sph` is large in terms of both time shift and waveform difference, even for small epicentral distances, along both meridians and parallels (Figure 9 and S5). When the source is on the edge of the UTM zone (Figure 7e, f), the receiver must be within 8 degrees of latitude or longitude away from the source to achieve a $\leq 8\%$ relative waveform difference (Figure 10 and S6). Considering a typical study where sources and receivers are randomly distributed in the study region, and taking the relative waveform difference of $\leq 10\%$ as a rough criterion of acceptable accuracy, we recommend that the size of the study region should not be larger than 8° as a rule of thumb for the UTM projection to produce reasonably accurate simulation results. For studies on regions larger than 8°, we recommend that the UTM projection should not be used and the curvature of the Earth should be accurately taken into account in order to guarantee accurate simulation results.

4.4. Accurate simulation of body waves

Despite our primary focus on surface wave simulations, we also examine the ability of the `Cube2sph` package to simulate body waves accurately in this section. As shown in Figure 4b, the body-wave waveforms with truncated `Cube2sph` mesh at 220 km depth and the Stacey boundary condition (red dashed lines) are significantly different from the one-chunk results (blue lines) for epicentral distances $> 8°$, suggesting that the mesh truncated at 220 km depth cannot be used to accurately simulate body-wave phases. This waveform contamination is most likely due to the artificial reflections from the bottom boundary and/or deep structures unaccounted for by the truncated mesh. Furthermore, the body-wave discrepancies observed between the one-chunk mesh (blue lines) and the global simulation results (green lines) indicate that reflections from the sides also contaminate body-wave phases similar to the surface waves, and therefore extending the computation domain to a larger depth alone cannot solve this issue for the Stacey boundary.

This is further confirmed when PML is applied to the `Cube2sph` mesh truncated at 220 km. In this case, while surface waves at the periods of $6 - 50$s can be accurately simulated (Figure 5a), some body waves still cannot be accurately computed before surface-wave arrivals (Figure 5b). This also suggests that in order to accurately simulate body waves, it is necessary to extend the computation domain downward to include deeper structures beneath 220 km. Figure 11 shows the simulation results using a mesh extended down to 670 km depth while keeping other parameters the same as in Section 4.2. It can be seen that by truncating the computation domain at 670 km depth and using PML, the simulation accuracy of the body-wave phases before the surface-wave arrivals is greatly improved for the epicentral distance ranges in the numerical experiment. If only Stacey boundary condition is applied to the 670-km depth-truncated mesh (red dashed lines as shown in Figure 12), while the overall waveforms are very similar to the one-chunk results (blue lines), significant differences can be observed in certain time ranges when compared to the global reference waveforms (green lines) based on `AxiSEM`, especially for epicentral distances $\geq 12°$. Compared with the PML waveforms obtained in Figure 11 which match well with the global results, it is clear that structures below 670 km should not be the reason for these differences. Therefore, the differences between the `Cube2sph` results and the one-chunk results in Figure 12 should be due to the artificial reflection from the bottom.

The numerical experiments presented in this section and in Figures 5b, 11-12 show that in order to accurately simulate the waveform of a specific phase, not only a good absorbing boundary is needed to suppress the artificial reflections, but the mesh also needs to have a deep enough truncation depth to include all the structures that are relevant to that phase, which varies with phase and period band. We recommend that for specific applications, the truncation depth should be determined according to the phase and period band of interest, and preferably, based on numerical tests.

5. Conclusion

We develop a toolkit, `Cube2sph`, that uses the "cubed sphere" transformation to generate continental-scale meshes that can honor the Earth's curvature for the open-source community-supported `SPECFEM3D_Cartesian` package used for seismic wave simulations. The toolkit also implements the curvilinear PML to absorb the outgoing waves at artificial boundaries. A series of numerical experiments are conducted to compare the waveforms using the `Cube2sph` mesh with PML and the Stacey boundary conditions with those using the `SPECFEM3D_GLOBE` one-chunk mesh and the `SPECFEM3D_Cartesian` UTM mesh, which demonstrate the effectiveness of the `Cube2sph` toolkit in continental-scale seismic wave simulations.

These numerical experiments show that using the `Cube2sph` mesh truncated at 220 km depth, the simulated surface waves (at the period band of $6-50$ s) are as accurate as those using the `SPECFEM3D_GLOBE` one-chunk mesh which extends into the inner core, with the number of elements reduced by a factor of 5. However, the Stacey boundary condition may not effectively absorb outgoing waves at grazing angles and results in artificial reflections from side boundaries that severely contaminate surface-wave signals. The curvilinear PML can be used to help effectively suppress artificial reflections which results in more accurate waveforms albeit with a longer computation time. Taking into consideration both the effectiveness of absorption and the computation time, using PML is more advantageous than running simulations on an enlarged domain with the Stacey boundary condition, at least for the source-receiver geometry and period band shown in the numerical experiments. Based on the numerical experiments, we recommend that the Earth's spherical geometry should be accurately considered, instead of approximated using the UTM projection, when the study region is larger than 8°. To accurately simulate body waves, both the PML boundary condition and a deeper truncation depth may be necessary.

In addition to accuracy, the `Cube2sph` toolkit, combined with the `SPECFEM3D_Cartesian` internal mesher or external meshing tools, can flexibly incorporate customized surface and interface topography, 3-D tomographic models and mesh refinement. With the accurate honoring of the spherical curvature and the corresponding curvilinear PML boundary condition, as well as the ability to flexibly accommodate complexities in the mesh, the combination of the `Cube2sph` toolkit and the `SPECFEM3D_Cartesian` is a more accurate and flexible alternative to the `SPECFEM3D_GLOBE` package for the applications of continental-scale simulations as well as subsequent full-waveform inversions.

6. Acknowledgments

The authors acknowledge that open-source visualization software Paraview and Python packages Numpy, SciPy, Matplotlib and Obspy are heavily used to produce the figures in this paper. The authors benefit from discussions with Dr. Carl Tape, Dr. Bryant Chow, Dr. Min Chen and Dr. Guoliang Li. T. Liu is funded by the Ontario Trillium Scholarship. Y. Xie acknowledges funding support from the Natural Environment Research Council (NE/M003507/1), the

European Research Council (GA 638665), and the National Science Foundation (NSF-EAR-2147918). C. A. Rychert and N. Harmon acknowledge funding from the Natural Environment Research Council (NERC) (grants NE/M003507/1 and NE/K010654/1) and the European Research Council (grant GA 638665). C. A. Rychert acknowledges funding from the National Science Foundation (grants NSF-EAR-2147918 and NSF-OCE-2316136). We thank the editor and three anonymous reviews for their constructive comments.

Code availability section

Name of the code/library: `Cube2sph`

Contact: tianshi.liu@mail.utoronto.ca, +1 647-804-3794

Hardware requirements: CPU cluster

Program language: Fortran, C, Python, Bash

Software required: Intel Fortran and C compiler, NetCDF, OpenMPI, Python3, Linux

Program size: 94MB

The source codes are available for downloading at the link: https://github.com/tianshi-liu/SPECFEM3D-with-Cube2sph-and-PML

References

Bérenger, J.P., 1999. Evanescent waves in PML's: Origin of the numerical reflection in wave-structure interaction problems. IEEE Transactions on Antennas and Propagation 47, 1497–1503. doi:10.1109/8.805891.

Berg, E.M., Lin, F.C., Allam, A., Schulte-Pelkum, V., Ward, K.M., Shen, W., 2020. Shear velocity model of alaska via joint inversion of rayleigh wave ellipticity, phase velocities, and receiver functions across the alaska transportable array. Journal of Geophysical Research: Solid Earth 125, e2019JB018582.

Casarotti, E., Stupazzini, M., Lee, S.J., Komatitsch, D., Piersanti, A., Tromp, J., 2008. Geocubit, an hpc parallel mesher for spectral-element method seismic wave simulation.

Chen, M., Niu, F., Liu, Q., Tromp, J., Zheng, X., 2015. Multiparameter adjoint tomography of the crust and upper mantle beneath East Asia: 1. Model construction and comparisons. Journal of Geophysical Research: Solid Earth 120, 1762–1786. doi:10.1002/2015JB012608.Received.

Clayton, R., Engquist, B., 1977. Absorbing boundary conditions for acoustic and elastic wave equations. Bulletin of the Seismological Society of America 67, 1529–1540.

Collino, F., Monk, P., 1998. The perfectly matched layer in curvilinear coordinates. Journal of Scientific Computing 19, 2061–2090.

Courant, R., Friedrichs, K., Lewy, H., 1928. Über die partiellen Differenzengleichungen der mathematischen Physik. Mathematische Annalen 100, 32–74. doi:10.1007/978-1-4612-5385-3_7.

Cupillard, P., Delavaud, E., Burgos, G., Festa, G., Vilotte, J.P., Capdeville, Y., Montagner, J.P., 2012. RegSEM: a versatile code based on the spectral element method to compute seismic wave propagation at the regional scale. Geophysical Journal International 188, 1203–1220. URL: https://doi.org/10.1111/j.1365-246X.2011.05311.x, doi:10.1111/j.1365-246X.2011.05311.x, arXiv:https://academic.oup.com/gji/article-pdf/188/3/1203/5947529/188-3-1203.pdf.

Dumbser, M., Käser, M., 2006. An arbitrary high-order discontinuous galerkin method for elastic waves on unstructured meshes—ii. the three-dimensional isotropic case. Geophysical Journal International 167, 319–336.

Dziewonski, A.M., Anderson, D.L., 1981. Preliminary reference Earth model. Physics of the Earth and Planetary Interiors 25, 297–356.

Festa, G., Vilotte, J.P., 2005. The Newmark scheme as velocity-stress time-staggering: An efficient PML implementation for spectral element simulations of elastodynamics. Geophysical Journal International 161, 789–812. doi:10.1111/j.1365-246X.2005.02601.x.

Fichtner, A., Kennett, B.L.N., Igel, H., Bunge, H.p., 2010. Full waveform tomography for radially anisotropic structure : New insights into present and past states of the Australasian upper mantle. Earth and Planetary Science Letters 290, 270–280. doi:10.1016/j.epsl.2009.12.003.

Gao, H., Zhang, J., 2008. Implementation of perfectly matched layers in an arbitrary geometrical boundary for elastic wave modelling. Geophysical Journal International 174, 1029–1036. doi:10.1111/j.1365-246X.2008.03883.x.

Gokhberg, A., Fichtner, A., 2016. Full-waveform inversion on heterogeneous HPC systems. Computers and Geosciences 89, 260–268.

Graves, R.W., 1998. Three-dimensional finite-difference modeling of the San Andreas fault: Source parameterization and ground-motion levels. Bulletin of the Seismological Society of America 88, 881–897.

Komatitsch, D., Liu, Q., Tromp, J., Süss, P., Stidham, C., Shaw, J.H., 2004. Simulations of Ground Motion in the Los Angeles Basin Based upon the Spectral-Element Method. Bulletin of the Seismological Society of America 94, 187–206. doi:10.1785/0120030077.

Komatitsch, D., Martin, R., 2007. An unsplit convolutional perfectly matched layer improved at grazing incidence for the seismic wave equation. Geophysics 72, SM155–SM167. URL: http://library.seg.org/doi/10.1190/1.2757586, doi:10.1190/1.2757586.

Komatitsch, D., Tromp, J., 1999. Introduction to the spectral element method for three-dimensional seismic wave propagation. Geophysical Journal International 139, 806–822. doi:10.1046/j.1365-246X.1999.00967.x.

Komatitsch, D., Tromp, J., 2002a. Spectral-element simulations of global seismic wave propagation - I. Validation. Geophysical Journal International 149, 390–412. doi:10.1046/j.1365-246X.2002.01653.x.

Komatitsch, D., Tromp, J., 2002b. Spectral-element simulations of global seismic wave propagation—II. Three-dimensional models, oceans, rotation and self-gravitation. Geophysical Journal International 149, 390–412. doi:10.1046/j.1365-246X.2002.01653.x.

Komatitsch, D., Tromp, J., 2003. A Perfectly Matched Layer absorbing boundary condition for the second-order seismic wave equation. Geophysical Journal International 154, 146–153. doi:10.1017/CBO9781107415324.004, arXiv:arXiv:1011.1669v3.

Laske, G., Masters, G., Ma, Z., Pasyanos, M., 2013. Update on crust1. 0—a 1-degree global model of earth's crust, in: Geophysical research abstracts, EGU General Assembly Vienna, Austria. p. 2658.

Li, G., Tao, K., Chen, M., Li, J., Maguire, R., Ma, X., 2022. Cartesian Meshing Spherical Earth (CMSE): A Code Package to Incorporate the Spherical Earth in SPECFEM3D Cartesian Simulations. Seismological Research Letters 93, 986–996. doi:10.1785/0220210131.

Liu, Q., Polet, J., Komatitsch, D., Tromp, J., 2004. Spectral-element moment tensor inversions for eathquakes in southern California. Bulletin of the Seismological Society of America 94, 1748–1761. doi:10.1785/012004038.

Liu, Q.H., 1999. Perfectly matched layers for elastic waves in cylindrical and spherical coordinates. The Journal of the Acoustical Society of America 105, 2075–2084. doi:10.1121/1.426812.

Martin, R., Komatitsch, D., 2009. An unsplit convolutional perfectly matched layer technique improved at grazing incidence for the viscoelastic wave equation. Geophysical Journal International 179, 333–344. doi:10.1111/j.1365-246X.2009.04278.x.

Martin, R., Komatitsch, D., Gedney, S.D., 2008. A variational formulation of a stabilized unsplit convolutional perfectly matched layer for the isotropic or anisotropic seismic wave equation. CMES - Computer Modeling in Engineering and Sciences 37, 274–304.

Martin, R., Komatitsch, D., Gedney, S.D., Bruthiaux, E., 2010. A high-order time and space formulation of the unsplit perfectly matched layer for the seismicwave equation using auxiliary differential equations (ADE-PML). CMES - Computer Modeling in Engineering and Sciences 56, 17–40.

Meza-Fajardo, K.C., Papageorgiou, A.S., 2008. A nonconvolutional, split-field, perfectly matched layer for wave propagation in isotropic and anisotropic elastic media: Stability analysis. Bulletin of the Seismological Society of America 98, 1811–1836. doi:10.1785/0120070223.

Nissen-Meyer, T., Van Driel, M., Stähler, S.C., Hosseini, K., Hempel, S., Auer, L., Colombi, A., Fournier, A., 2014. AxiSEM: Broadband 3-D seismic wavefields in axisymmetric media, in: Solid Earth, pp. 425–445. doi:10.5194/se-5-425-2014.

Pellegrini, F., 2010. Scotch and libScotch 5.1 user's guide. Technical Report. URL: http://hal.archives-ouvertes.fr/hal-00410327/.

Pitarka, A., 1999. 3D Elastic finite-difference modeling of seismic motion using staggered grids with nonuniform spacing. Bulletin of the Seismological Society of America 89, 54–68.

Ponce, M., Van Zon, R., Northrup, S., Gruner, D., Chen, J., Ertinaz, F., Fedoseev, A., Groer, L., Mao, F., Mundim, B.C., Nolta, M., Pinto, J., Saldarriaga, M., Slavnic, V., Spence, E., Yu, C.H., Peltier, W.R., 2019. Deploying a top-100 supercomputer for large parallel workloads: The Niagara supercomputer, in: ACM International Conference Proceeding Series. doi:10.1145/3332186.3332195, arXiv:1907.13600.

Ritsema, J., Deuss, A., van Heijst, H.J., Woodhouse, J.H., 2011. S40RTS: a degree-40 shear-velocity model for the mantle from new Rayleigh wave dispersion, teleseismic traveltime and normal-mode splitting function measurements. Geophysical Journal International 184, 1223–1236. URL: https://doi.org/10.1111/j.1365-246X.2010.04884.x, doi:10.1111/j.1365-246X.2010.04884.x, arXiv:https://academic.oup.com/gji/article-pdf/184/3/1223/1744253/184-3-1223.pdf.

Ronchi, C., Iacono, R., Paolucci, P.S., 1996. The "Cubed sphere": A new method for the solution of partial differential equations in spherical geometry. Journal of Computational Physics 124, 93–114.

Snyder, J.P., 1982. Map projections used by the U.S. Geological Survey. Technical Report. Washington, D.C.

Tao, K., Grand, S.P., Niu, F., 2018. Seismic Structure of the Upper Mantle Beneath Eastern Asia From Full Waveform Seismic Tomography. Geochemistry, Geophysics, Geosystems 19, 2732–2763. doi:10.1029/2018GC007460.

Tape, C., Liu, Q., Maggi, A., Tromp, J., 2010. Seismic tomography of the southern California crust based on spectral-element and adjoint methods. Geophysical Journal International 180, 433–462.

Tromp, J., Komatitsch, D., Hjörleifsdóttir, V., Liu, Q., Zhu, H., Peter, D., Bozdag, E., McRitchie, D., Friberg, P., Trabant, C., Hutko, A., 2010. Near real- time simulations of global CMT earthquakes. Geophysical Journal International 183, 381–389. doi:10.1111/j.1365-246X.2010.04734.x.

Tromp, J., Komatitsch, D., Liu, Q., 2008. Spectral-element and adjoint methods in seismology. Communications in Computational Physics 3, 1–32.

Wang, K., Liu, Q., Yang, Y., 2019. Three-Dimensional Sensitivity Kernels for Multicomponent Empirical Green's Functions From Ambient Noise: Methodology and Application to Adjoint Tomography. Journal of Geophysical Research: Solid Earth doi:10.1029/2018JB017020.

Wang, S., Lee, R., Teixeira, F.L., 2004. Anisotropic-medium PML for FETD with conjugate-scaled basis functions. IEEE Antennas and Propagation Society, AP-S International Symposium (Digest) 4, 3485–3488. doi:10.1109/aps.2004.1330096.

Wang, X., Zhan, Z., 2020. Moving from 1-D to 3-D velocity model: Automated waveform-based earthquake moment tensor inversion in the Los Angeles region. Geophysical Journal International 220, 218–234. doi:10.1093/gji/ggz435.

Xie, Z., Komatitsch, D., Martin, R., Matzen, R., 2014. Improved forward wave propagation and adjoint-based sensitivity kernel calculations using a numerically stable finite-element PML. Geophysical Journal International 198, 1714–1747. doi:10.1093/gji/ggu219.

Zhang, J., Gao, H., 2011. Irregular perfectly matched layers for 3D elastic wave modeling. Geophysics 76. doi:10.1190/1.3533999.

Zhang, W., Shen, Y., 2010. Unsplit complex frequency-shifted PML implementation using auxiliary differential equations for seismic wave modeling. Geophysics 75. doi:10.1190/1.3463431.

Zhang, Z., Zhang, W., Chen, X., 2014. Complex frequency-shifted multi-axial perfectly matched layer for elastic wave modelling on curvilinear grids. Geophysical Journal International 198, 140–153. doi:10.1093/gji/ggu124.

Zhao, B., Kagawa, T., Turugi, M., 2007. Study on long-period strong motion simulation for large-scale earthquakes. Journal of Geophysics and Engineering 4, 301–307.

Zhu, H., Bozdăg, E., Tromp, J., 2015. Seismic structure of the European upper mantle based on adjoint tomography. Geophysical Journal International 201, 18–52.

A. The spectral-element formulation of the curvilinear-grid PML using auxiliary differential equation

Let us start from the velocity-stress formulation of the elastodynamic equation

$$\begin{aligned} \rho \frac{\partial \boldsymbol{v}}{\partial t} &= \nabla \cdot \boldsymbol{\sigma} + \boldsymbol{f}, \\ \frac{\partial \boldsymbol{\sigma}}{\partial t} &= \boldsymbol{C} : \nabla \boldsymbol{v}, \end{aligned} \tag{4}$$

in which $\boldsymbol{v}$, $\boldsymbol{\sigma}$ and $\boldsymbol{f}$ are velocity, stress and body force, respectively. ρ is the density, and $\boldsymbol{C}$ is the 4-th order elastic tensor. For PML implementation in Cartesian grids, the differential operator ∇ is replaced in the PML domain by $\tilde{\nabla}$, which is defined by

$$\tilde{\nabla} a = \mathcal{F}^{-1} \left\{ \boldsymbol{S} \cdot \nabla \hat{a} \right\}, \tag{5}$$

in which a is an arbitrary function of space and time, $\mathcal{F}^{-1}$ is the inverse Fourier transform in time domain and $\hat{a}$ denotes the Fourier transform of a in time domain. The tensor $\boldsymbol{S}$ is the attenuation operator defined by

$$\boldsymbol{S} = \frac{\hat{\boldsymbol{e}}_x \hat{\boldsymbol{e}}_x}{s_x(x)} + \frac{\hat{\boldsymbol{e}}_y \hat{\boldsymbol{e}}_y}{s_y(y)} + \frac{\hat{\boldsymbol{e}}_z \hat{\boldsymbol{e}}_z}{s_z(z)}, \tag{6}$$

in which

$$\begin{aligned} s_x(x) &= \kappa_x(x) + \frac{d_x(x)}{\alpha_x(x) + \mathrm{i}\omega}, \\ s_y(y) &= \kappa_y(y) + \frac{d_y(y)}{\alpha_y(y) + \mathrm{i}\omega}, \\ s_z(z) &= \kappa_z(z) + \frac{d_z(z)}{\alpha_z(z) + \mathrm{i}\omega}, \end{aligned} \tag{7}$$

where κ_i, α_i and d_i, $i = x, y, z$ are user-defined parameters.

In curvilinear grids, we derive the PML formulations using the transformation from the curvilinear coordinates (ξ, η, ζ) to the Cartesian coordinates (x, y, z). We denote the gradient in (ξ, η, ζ) as ∇_ξ, and the second-order Jacobian tensor, $\boldsymbol{\mathcal{R}}$, written as

$$\begin{aligned} \boldsymbol{\mathcal{R}} = \hat{\boldsymbol{e}}_\xi \Big(&\frac{\partial x}{\partial \xi} \hat{\boldsymbol{e}}_x + \frac{\partial y}{\partial \xi} \hat{\boldsymbol{e}}_y + \frac{\partial z}{\partial \xi} \hat{\boldsymbol{e}}_z\Big) \\ + \hat{\boldsymbol{e}}_\eta \Big(&\frac{\partial x}{\partial \eta} \hat{\boldsymbol{e}}_x + \frac{\partial y}{\partial \eta} \hat{\boldsymbol{e}}_y + \frac{\partial z}{\partial \eta} \hat{\boldsymbol{e}}_z\Big) \\ + \hat{\boldsymbol{e}}_\zeta \Big(&\frac{\partial x}{\partial \zeta} \hat{\boldsymbol{e}}_x + \frac{\partial y}{\partial \zeta} \hat{\boldsymbol{e}}_y + \frac{\partial z}{\partial \zeta} \hat{\boldsymbol{e}}_z\Big), \end{aligned} \tag{8}$$

will give

$$\nabla_\xi a = \boldsymbol{\mathcal{R}} \cdot \nabla a \tag{9}$$

for any function a. Motivated by eqn. (5), in order to impose attenuation along (ξ, η, ζ) directions, we define $\tilde{\nabla}_\xi$ as

$$\tilde{\nabla}_\xi a = \mathcal{F}^{-1}\left\{\boldsymbol{S'} \cdot \nabla_\xi \hat{a}\right\} \tag{10}$$

to replace ∇_ξ in the PML domain. Similarly,

$$\boldsymbol{S'} = \frac{\hat{\boldsymbol{e}}_\xi \hat{\boldsymbol{e}}_\xi}{s_\xi(\xi)} + \frac{\hat{\boldsymbol{e}}_\eta \hat{\boldsymbol{e}}_\eta}{s_\eta(\eta)} + \frac{\hat{\boldsymbol{e}}_\zeta \hat{\boldsymbol{e}}_\zeta}{s_\zeta(\zeta)}, \tag{11}$$

and

$$\begin{aligned} s_\xi(\xi) &= \kappa_\xi(\xi) + \frac{d_\xi(\xi)}{\alpha_\xi(\xi) + \mathrm{i}\omega}, \\ s_\eta(\eta) &= \kappa_\eta(\eta) + \frac{d_\eta(\eta)}{\alpha_\eta(\eta) + \mathrm{i}\omega}, \\ s_\zeta(\zeta) &= \kappa_\zeta(\zeta) + \frac{d_\zeta(\zeta)}{\alpha_\zeta(\zeta) + \mathrm{i}\omega}. \end{aligned} \tag{12}$$

Combining eqn. (9) and eqn. (10), we can define $\tilde{\nabla}$ in the PML domain as

$$\tilde{\nabla} a = \boldsymbol{\mathcal{R}}^{-1} \cdot \tilde{\nabla}_\xi a = \mathcal{F}^{-1}\left\{\boldsymbol{\mathcal{R}}^{-1} \cdot \boldsymbol{S'} \cdot \boldsymbol{\mathcal{R}} \cdot \nabla \hat{a}\right\} \tag{13}$$

to replace the differential operator ∇ in eqn. (4), and by furthering denoting

$$\begin{aligned} \boldsymbol{\mathcal{R}} &= \hat{\boldsymbol{e}}_\xi \boldsymbol{r}_\xi + \hat{\boldsymbol{e}}_\eta \boldsymbol{r}_\eta + \hat{\boldsymbol{e}}_\zeta \boldsymbol{r}_\zeta, \\ \boldsymbol{\mathcal{R}}^{-1} &= \boldsymbol{r}_\xi^{-1} \hat{\boldsymbol{e}}_\xi + \boldsymbol{r}_\eta^{-1} \hat{\boldsymbol{e}}_\eta + \boldsymbol{r}_\zeta^{-1} \hat{\boldsymbol{e}}_\zeta, \end{aligned} \tag{14}$$

we can rewrite the velocity-stress equation as

$$\begin{aligned} \rho \frac{\partial \boldsymbol{v}}{\partial t} &= \mathcal{F}^{-1}\left\{\frac{1}{s_\xi}(\boldsymbol{r}_\xi^{-1}\boldsymbol{r}_\xi) : \nabla\hat{\boldsymbol{\sigma}} + \frac{1}{s_\eta}(\boldsymbol{r}_\eta^{-1}\boldsymbol{r}_\eta) : \nabla\hat{\boldsymbol{\sigma}} + \frac{1}{s_\zeta}(\boldsymbol{r}_\zeta^{-1}\boldsymbol{r}_\zeta) : \nabla\hat{\boldsymbol{\sigma}}\right\} + \boldsymbol{f}, \\ \frac{\partial \boldsymbol{\sigma}}{\partial t} &= \mathcal{F}^{-1}\left\{\frac{1}{s_\xi}\boldsymbol{C} : (\boldsymbol{r}_\xi^{-1}\boldsymbol{r}_\xi \cdot \nabla\hat{\boldsymbol{v}}) + \frac{1}{s_\eta}\boldsymbol{C} : (\boldsymbol{r}_\eta^{-1}\boldsymbol{r}_\eta \cdot \nabla\hat{\boldsymbol{v}}) + \frac{1}{s_\zeta}\boldsymbol{C} : (\boldsymbol{r}_\zeta^{-1}\boldsymbol{r}_\zeta \cdot \nabla\hat{\boldsymbol{v}})\right\}. \end{aligned} \tag{15}$$

Note that $\boldsymbol{\mathcal{R}}$ and $\boldsymbol{\mathcal{R}}^{-1}$ are defined on GLL points, and can be numerically computed via interpolation using the (ξ, η, ζ)

and (x, y, z) coordinates of GLL points. The inverse Fourier transform in eqn. (15) can be evaluated as (Martin et al., 2010)

$$\mathcal{F}^{-1}\left\{\frac{\hat{a}}{s_\lambda}\right\} = \frac{a}{\kappa_\lambda} + Q^a_\lambda, \quad \text{for } \lambda = \xi, \eta, \zeta \tag{16}$$

and Q^a_λ can be solved with an auxiliary differential equation (e.g., Martin et al., 2010)

$$\frac{\partial Q^a_\lambda}{\partial t} = -\beta_\lambda Q^a_\lambda - \frac{d_\lambda}{\kappa^2_\lambda} a, \tag{17}$$

in which

$$\beta_\lambda = \alpha_\lambda + \frac{d_\lambda}{\kappa_\lambda}. \tag{18}$$

Substituting eqn. (16) and eqn. (17) into eqn. (15), we obtain the velocity-stress formulation in the PML domain

$$\rho\frac{\partial \boldsymbol{v}}{\partial t} = \left(\frac{\boldsymbol{r}_\xi^{-1}\boldsymbol{r}_\xi}{\kappa_\xi} + \frac{\boldsymbol{r}_\eta^{-1}\boldsymbol{r}_\eta}{\kappa_\eta} + \frac{\boldsymbol{r}_\zeta^{-1}\boldsymbol{r}_\zeta}{\kappa_\zeta}\right) : \nabla\boldsymbol{\sigma} + \boldsymbol{Q}^{\boldsymbol{V}}_\xi + \boldsymbol{Q}^{\boldsymbol{V}}_\eta + \boldsymbol{Q}^{\boldsymbol{V}}_\zeta + \boldsymbol{f}, \tag{19}$$

$$\frac{\partial \boldsymbol{\sigma}}{\partial t} = \boldsymbol{C} : \left(\left(\frac{\boldsymbol{r}_\xi^{-1}\boldsymbol{r}_\xi}{\kappa_\xi} + \frac{\boldsymbol{r}_\eta^{-1}\boldsymbol{r}_\eta}{\kappa_\eta} + \frac{\boldsymbol{r}_\zeta^{-1}\boldsymbol{r}_\zeta}{\kappa_\zeta}\right) \cdot \nabla\boldsymbol{v}\right) + \boldsymbol{Q}^{\boldsymbol{\Sigma}}_\xi + \boldsymbol{Q}^{\boldsymbol{\Sigma}}_\eta + \boldsymbol{Q}^{\boldsymbol{\Sigma}}_\zeta \tag{20}$$

in which $\boldsymbol{Q}^{\boldsymbol{V}}_\lambda$ and $\boldsymbol{Q}^{\boldsymbol{\Sigma}}_\lambda$ $(\lambda = \xi, \eta, \zeta)$ can be solved by the auxiliary differential equations

$$\frac{\partial \boldsymbol{Q}^{\boldsymbol{V}}_\lambda}{\partial t} = -\beta_\lambda \boldsymbol{Q}^{\boldsymbol{V}}_\lambda - \frac{d_\lambda}{\kappa^2_\lambda}(\boldsymbol{r}_\lambda^{-1}\boldsymbol{r}_\lambda) : \nabla\boldsymbol{\sigma}, \tag{21}$$

$$\frac{\partial \boldsymbol{Q}^{\boldsymbol{\Sigma}}_\lambda}{\partial t} = -\beta_\lambda \boldsymbol{Q}^{\boldsymbol{\Sigma}}_\lambda - \frac{d_\lambda}{\kappa^2_\lambda}\boldsymbol{C} : (\boldsymbol{r}_\lambda^{-1}\boldsymbol{r}_\lambda \cdot \nabla\boldsymbol{v}). \tag{22}$$

Note that in spectral-element implementation, eqs. (19) and (21) should be solved in the weak form. Multiplying a test function $\phi(\boldsymbol{x})$ on eqs. (19) and (21), integrating over the whole computational domain Ω and the PML domain Ω_δ, as shown in Figure 13, respectively, and using integration by parts, we can obtain the weak form

$$\begin{aligned}\frac{\partial}{\partial t}\int_\Omega \phi\,\rho\boldsymbol{v}\mathrm{d}V = &-\int_\Omega \nabla\cdot\left(\phi\left(\frac{\boldsymbol{r}_\xi^{-1}\boldsymbol{r}_\xi}{\kappa_\xi} + \frac{\boldsymbol{r}_\eta^{-1}\boldsymbol{r}_\eta}{\kappa_\eta} + \frac{\boldsymbol{r}_\zeta^{-1}\boldsymbol{r}_\zeta}{\kappa_\zeta}\right)\right)\cdot\boldsymbol{\sigma}\mathrm{d}V \\ &+ \int_\Omega \phi\left(\boldsymbol{Q}^{\boldsymbol{V}}_\xi + \boldsymbol{Q}^{\boldsymbol{V}}_\eta + \boldsymbol{Q}^{\boldsymbol{V}}_\zeta + \boldsymbol{f}\right)\mathrm{d}V,\end{aligned} \tag{23}$$

$$\frac{\partial}{\partial t}\int_{\Omega_\delta}\phi \boldsymbol{Q}^{\boldsymbol{V}}_\lambda \mathrm{d}V = -\int_{\Omega_\delta}\phi\beta_\lambda \boldsymbol{Q}^{\boldsymbol{V}}_\lambda \mathrm{d}V - \int_{\partial\Omega_\delta}\phi\frac{d_\lambda}{\kappa_\lambda^2}(\boldsymbol{r}_\lambda^{-1}\boldsymbol{r}_\lambda) : \hat{\boldsymbol{n}}\boldsymbol{\sigma}\mathrm{d}S + \int_{\Omega_\delta}\nabla\cdot\left(\phi\frac{d_\lambda}{\kappa_\lambda^2}(\boldsymbol{r}_\lambda^{-1}\boldsymbol{r}_\lambda)\right)\cdot\boldsymbol{\sigma}\mathrm{d}V, \tag{24}$$

in which $\hat{\boldsymbol{n}}$ is the out-pointing normal vector on the boundary. The boundary of Ω contains two parts: the free surface Γ_0 and the outer boundary of the PML domain Γ_1, as shown in Figure 13. For eqn. (23), the following boundary condition is applied to

$$\left(\hat{\boldsymbol{n}}\cdot\left(\frac{\boldsymbol{r}_\xi^{-1}\boldsymbol{r}_\xi}{\kappa_\xi}+\frac{\boldsymbol{r}_\eta^{-1}\boldsymbol{r}_\eta}{\kappa_\eta}+\frac{\boldsymbol{r}_\zeta^{-1}\boldsymbol{r}_\zeta}{\kappa_\zeta}\right)\cdot\boldsymbol{\sigma}\right)\Bigg|_{\Gamma_0} = 0, \tag{25}$$

$$\boldsymbol{v}|_{\Gamma_1} = 0. \tag{26}$$

Outside the PML domain (as shown in Figure 13), we have $\kappa_\xi = \kappa_\eta = \kappa_\zeta = 1$, and since $\boldsymbol{r}_\xi^{-1}\boldsymbol{r}_\xi + \boldsymbol{r}_\eta^{-1}\boldsymbol{r}_\eta + \boldsymbol{r}_\zeta^{-1}\boldsymbol{r}_\zeta = \mathrm{I}$, eqn. (25) is reduced to $(\hat{\boldsymbol{n}}\cdot\boldsymbol{\sigma})|_{\Gamma_0\backslash\Omega_\delta} = 0$, i.e., the traction-free boundary condition. Since no spatial derivative of $\boldsymbol{Q}^{\boldsymbol{V}}_\lambda$ is involved in Eqn. (24), no boundary condition needs to be assigned to solve it.

In practice, the damping parameters κ_λ, d_λ, α_λ, $\lambda = \xi,\eta,\zeta$ in eqn. (12) can be chosen as (e.g., Zhang and Shen, 2010)

$$\begin{aligned}\kappa_\lambda &= 1 + (\kappa_0 - 1)\left(\frac{\delta\lambda}{L}\right)^{N_\kappa},\\ d_\lambda &= d_0\left(\frac{\delta\lambda}{L}\right)^{N_d},\\ \alpha_\lambda &= \alpha_0\left(1-\left(\frac{\delta\lambda}{L}\right)^{N_\alpha}\right),\end{aligned} \tag{27}$$

where $\delta\lambda$ is the distance to the inner boundary of the PML domain (as shown in Figure 13), L is the thickness of the PML domain, and N_κ, N_d and N_α are user-selected power factors. In our numerical experiments, we choose

$$\kappa_0 = 1,\quad N_d = 1.0,\quad d_0 = -\frac{(N_d+1.0)V_{p0}\ln\ R_{coef}}{2L},\quad \alpha_0 = \pi f_0,\quad N_\alpha = 1.0,\quad N_\kappa = 1.0,$$

where $f_0 = 0.2$ Hz, V_{p0} is the maximum P velocity, and $R_{coef} = 0.001$.

List of Figures

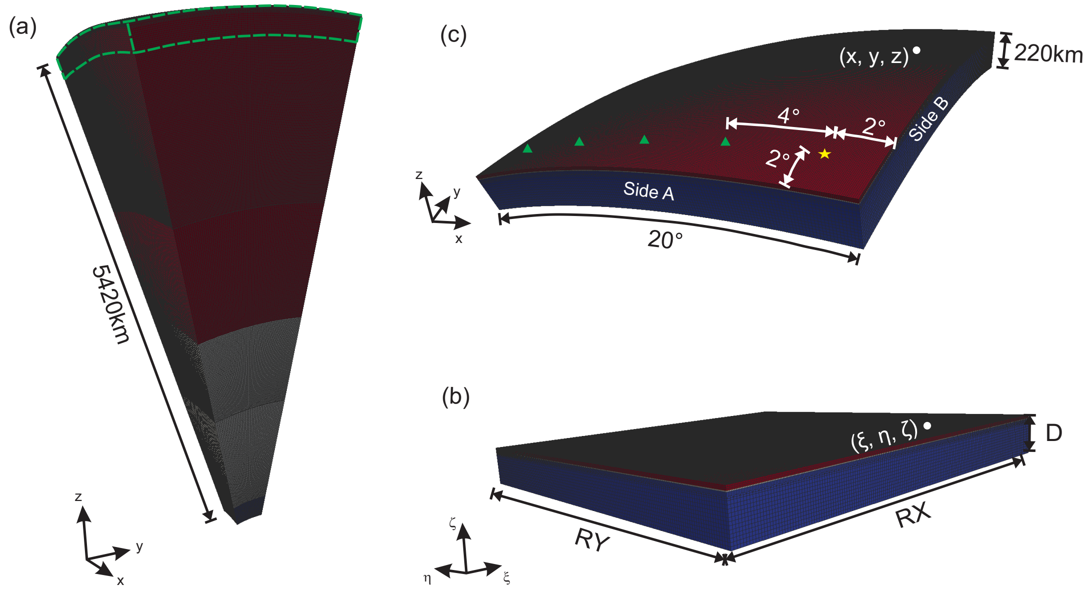

Figure 1: (a) The SPECFEM3D_GLOBE one-chunk mesh with horizontal size of $20° \times 20°$, extending down to $5420\,\mathrm{km}$ depth, which is inside the inner-core. Four doubling layers are implemented to accommodate the velocity increase with depth and to ensure that the element size does not shrink too much at deeper depth. (b) The cube-shaped mesh generated by the internal mesher of SPECFEM3D_Cartesian. (c) Cube2sph mesh with horizontal size of $20° \times 20°$, truncated at $220\,\mathrm{km}$ depth, identical to the upper-most part of the SPECFEM3D_GLOBE one-chunk mesh, marked by the green dashed line in (a). The yellow star and the green triangles mark the locations of source and receivers in the numerical tests carried out in this study. The elements are colored according to values of shear velocity, with red colors representing low velocity, blue colors representing high velocity.

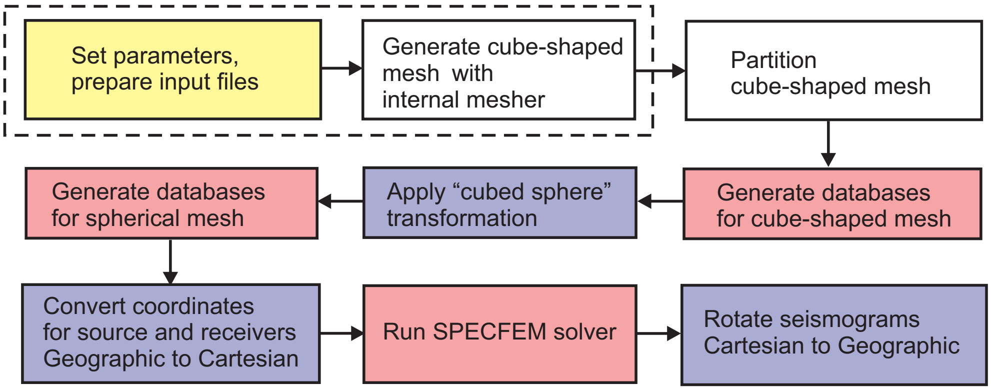

Figure 2: A flowchart showing the general procedure to use the `Cube2sph` package. The blocks represent the steps to build a cube-shaped mesh (first row), apply the "cubed sphere" transformation and generate mesh databases (second row), and launch the `SPECFEM` solver (third row), color-coded by the type of script/program used in each step: parameter setup and file preparation (yellow), original `SPECFEM` program (white), modified `SPECFEM` program (red) and utility scripts/programs (blue). Parameters need to be set before running the mesher include mesh size, number of elements, truncation depth, vertical layering, doubling layers and PML layers. Interface files and tomographic model files need to be prepared. The steps enclosed by the black dashed line may be different when an external mesher is used to build the cube-shaped mesh.

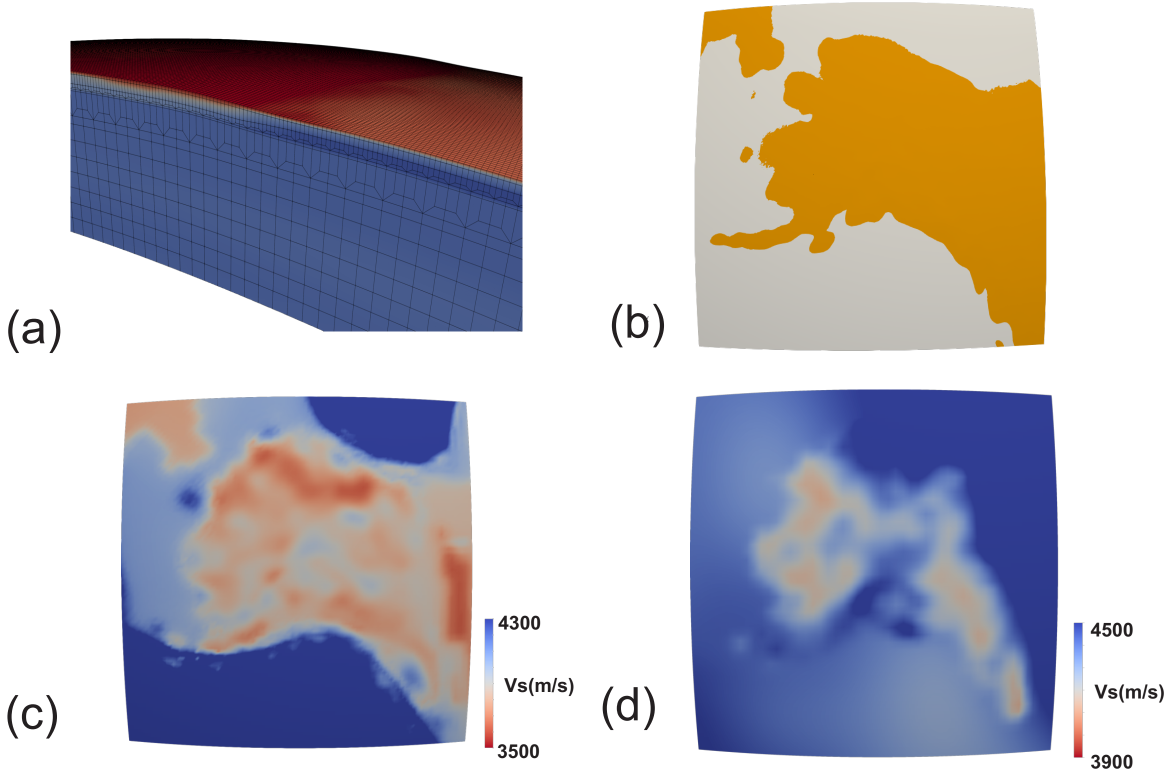

Figure 3: The final mesh and the structural model for Alaska. (a) A zoomed-in view of the grid, showing the mesh doubling and the honoring of the Moho topography. The elements are colored by shear velocity values, with warm colors representing low velocities. (b) The mesh masked by sea level. The yellow and white parts represent the areas above and below sea level. The outline of the yellow region follows the shape of the coastline of Alaska, indicating that the topography is correctly incorporated. (c) and (d) are shear velocity maps at $25\,\mathrm{km}$ and $90\,\mathrm{km}$ depths, with warm colors representing low shear velocities. The smooth background is S40RTS + Crust1.0, and the fine structures are the imprinted Berg et al. (2020) tomographic model.

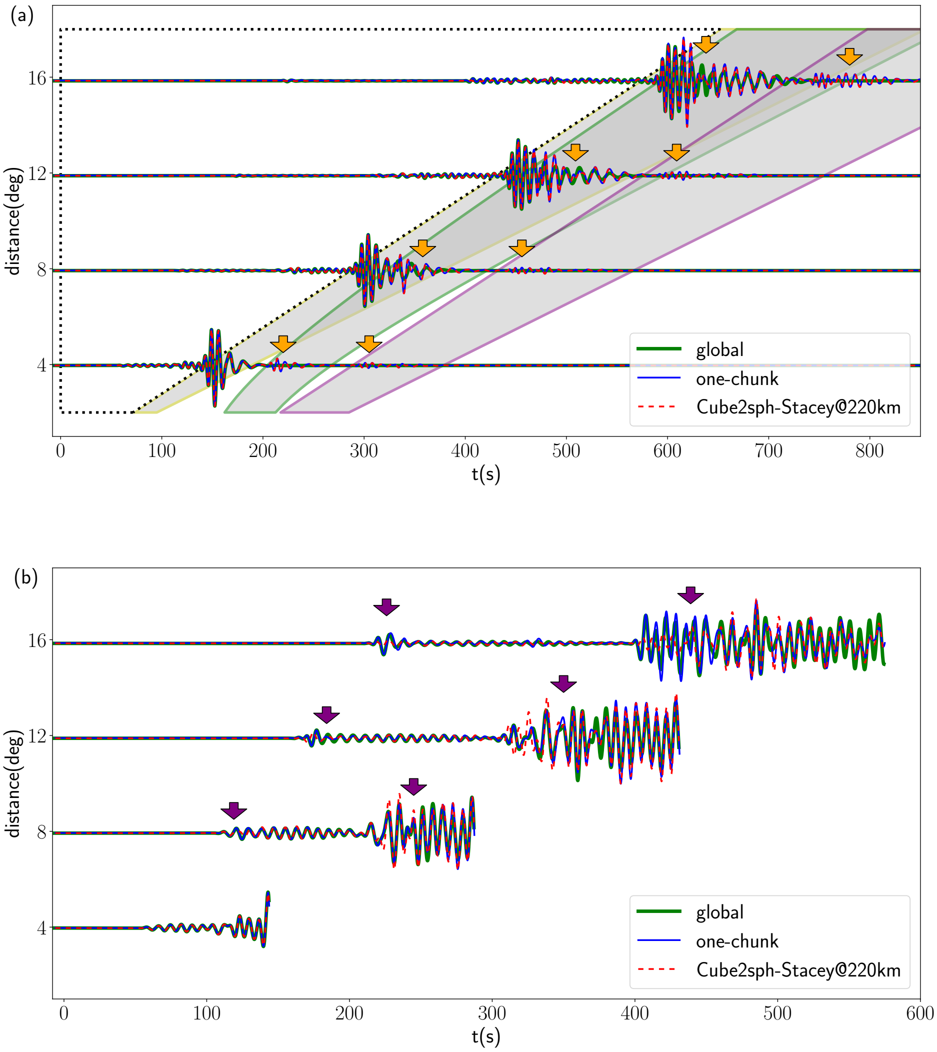

Figure 4: Comparison of waveforms simulated using the SPECFEM3D_GLOBE one-chunk mesh (blue lines) and the Cube2sph mesh (red dashed lines), with the whole-globe simulation result obtained by AxiSEM (thick green lines) displayed as background. (b) is a zoom-in view of (a) before the surface-wave arrivals (black dotted contour). All waveforms are filtered between $12 - 25\,\mathrm{s}$, and normalized according to the maximum amplitude of the global simulation waveforms (thick green lines). The shaded areas in (a) represent the time range of direct surface-wave arrival (yellow contour), artificial surface-wave reflection at side A (green contour) and at side B (purple contour) as marked in Figure 1, assuming a minimum and maximum group velocity of $v_{min} = 0.021°/\mathrm{s}$ and $v_{max} = 0.028°/\mathrm{s}$ for the period band of interest. Surface-wave signals are identical using the one-chunk mesh and the Cube2sph mesh, indicating that vertical truncation at $220\,\mathrm{km}$ affects very little surface-wave modeling. For body-wave waveforms, discrepancies can be observed between the Cube2sph and one-chunk results (purple arrows in b), indicating that truncating the mesh at $220\,\mathrm{km}$ affects body-wave modeling. Differences are also found between the Cube2sph/one-chunk and global results (orange arrows in a), due to the contamination of artificial reflections at the sides.

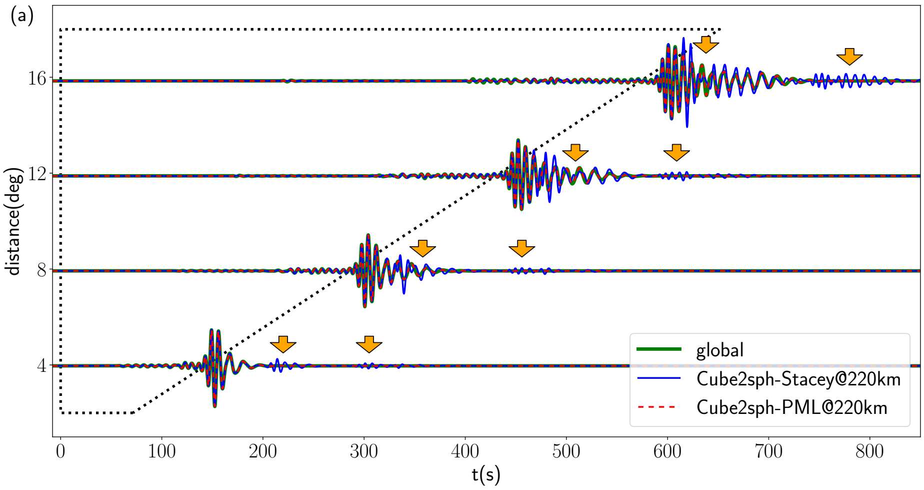

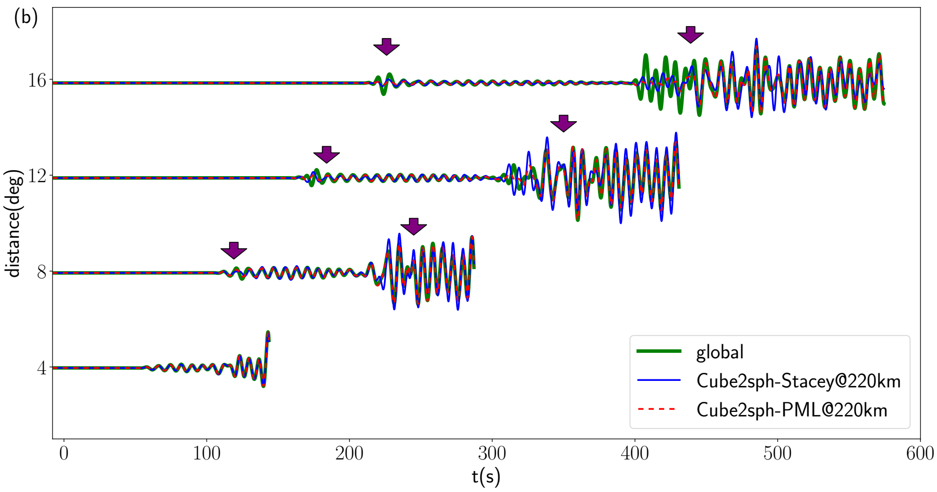

Figure 5: Comparison of waveforms simulated using the `Cube2sph` mesh with the Stacey boundary condition (blue lines) and PML boundaries (red dashed lines). The whole-globe simulation results obtained by `AxiSEM` (thick green lines) are displayed as background. (b) is a zoom-in view of (a) before the surface-wave arrivals (black dotted contour). The orange arrows in (a) point to the parts in surface-wave waveforms where artificial reflections of the Stacey boundary conditions can be observed. The purple arrows in (b) indicate the discrepancies between `AxiSEM` and `Cube2sph` in body-wave waveforms. It can be observed in (a) that with PML, surface-wave signals can be accurately simulated and the artificial reflections can be well suppressed. Body-wave phases cannot be accurately modeled even using PML boundaries, indicating that structures deeper than $220\,\mathrm{km}$ affect the body-wave signals.

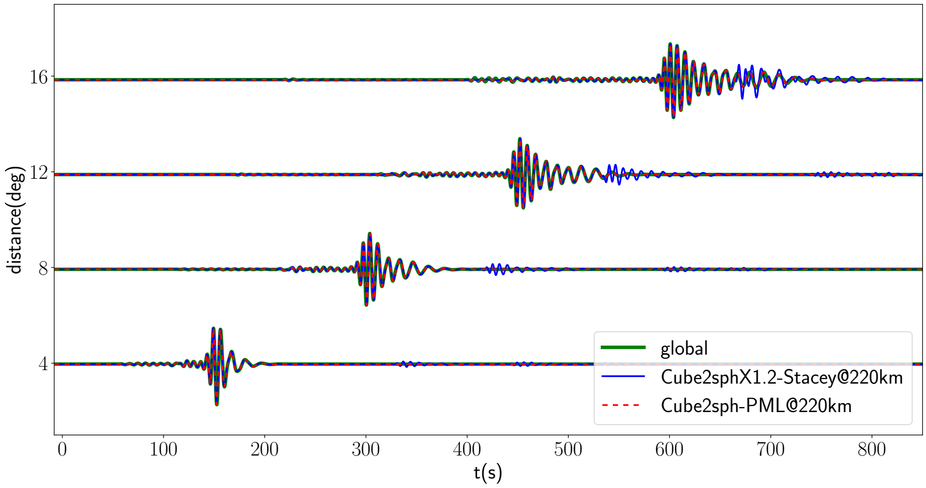

Figure 6: Comparison of waveforms simulated using the enlarged `Cube2sph` mesh with the Stacey boundary condition (blue lines) and using the original `Cube2sph` mesh with PML boundaries (red dashed lines). The whole-globe simulation results obtained by AxiSEM (thick green lines) are displayed as background. The artificial reflections are alleviated by enlarging the computation domain. However, they remain clearly visible especially for epicentral distances of $\geq 12^{\circ}$.

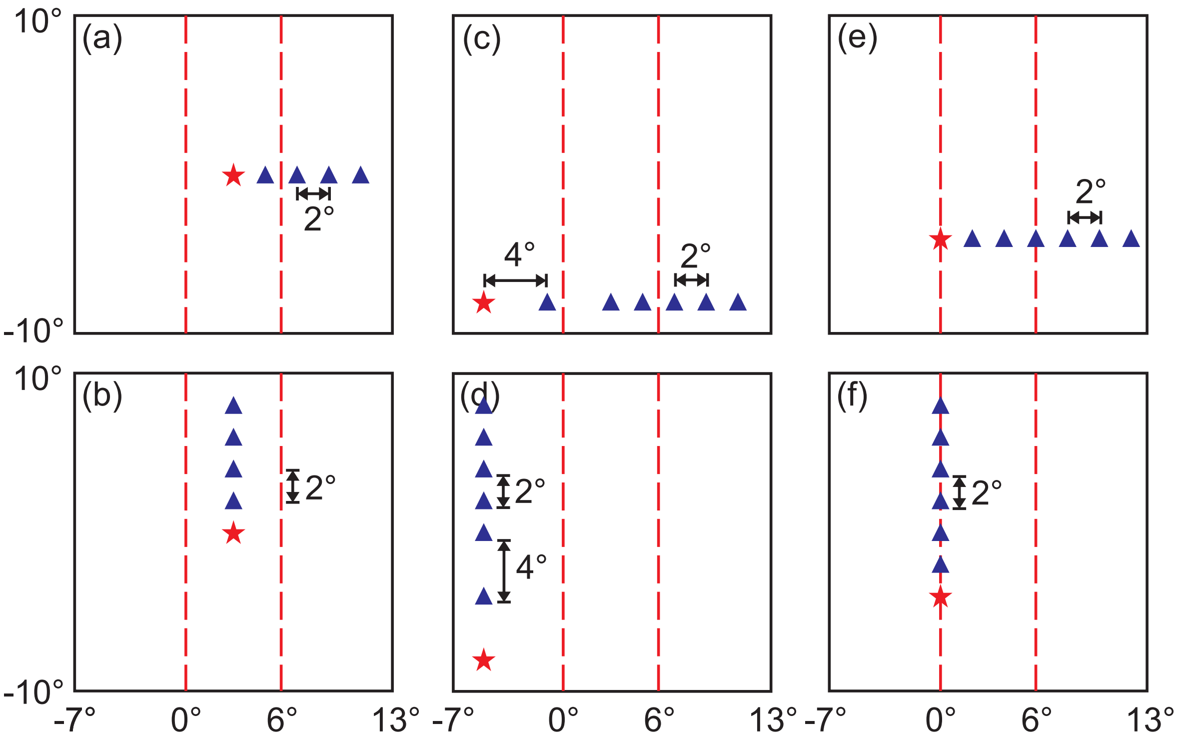

Figure 7: Locations of sources (red stars) and receivers (blue triangles) used in the numerical experiments to compare the `Cube2sph` and the UTM mesh. The meshes are centered at $(0°, 3°E)$, which is the center of UTM zone 31, marked by the red dotted lines. The size of the mesh is $20° \times 20°$. In (a) and (b), the sources are at the center of the meshes, which is also the center of the UTM zone which the UTM mesh is projected to. In (c) and (d), the sources are at the southwest corner of the mesh, which is outside the UTM zone which the mesh is projected to. In (e) and (f), the sources are on the west edge of the UTM zone which the mesh is projected to. In (a), (c) and (e), the receivers align to the east of the sources, and in (b), (d) and (f), the receivers align to the north of the sources.

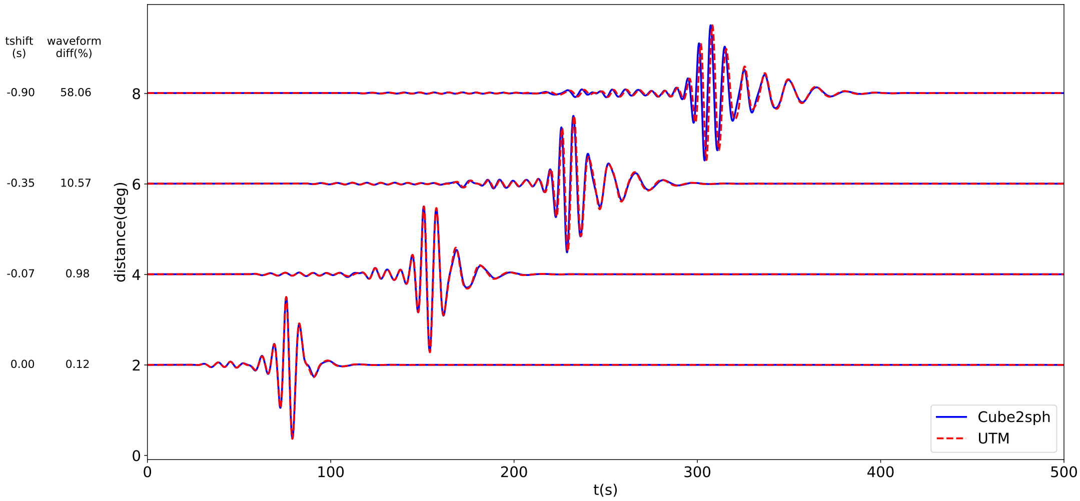

Figure 8: Waveforms generated by the `Cube2sph` (blue) and the UTM (red) meshes. The source is at the center of the meshes, which is also the center of the UTM zone which the UTM mesh is projected to, and the receivers align to the east of the source (Figure 7a). The numbers on the left of the waveforms are the relative waveform difference eqn. (3) and the cross-correlation time shift between the `Cube2sph` and the UTM results as two measurements of discrepancy between two methods.

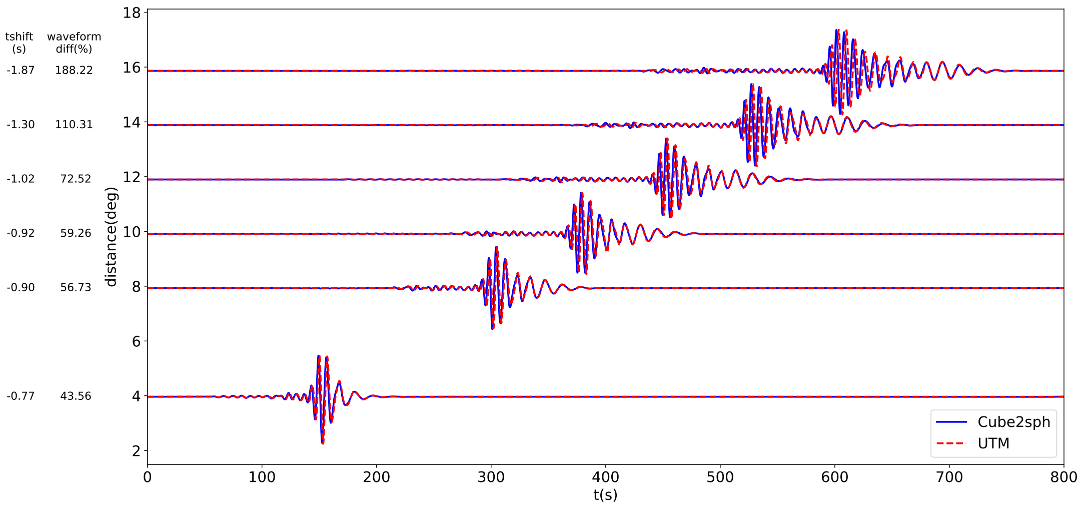

Figure 9: Same as Figure 8 except that the source is at the southwest corner of the meshes, which is outside the UTM zone which the UTM mesh is projected to, and the receivers align to the east of the source (Figure 7c).

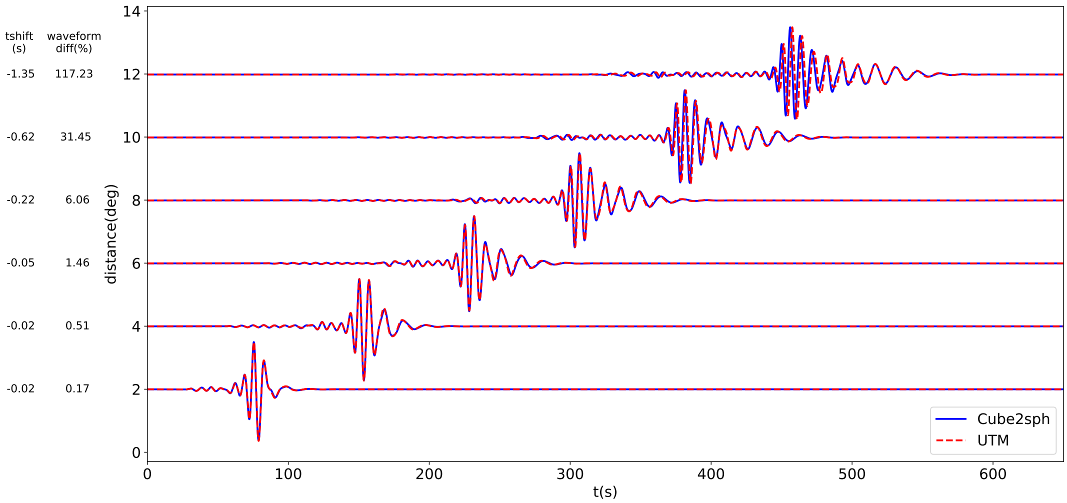

Figure 10: Same as Figure 8 except that the source is at the west edge of the UTM zone which the UTM mesh is projected to, and the receivers align to the east of the source (Figure 7e).

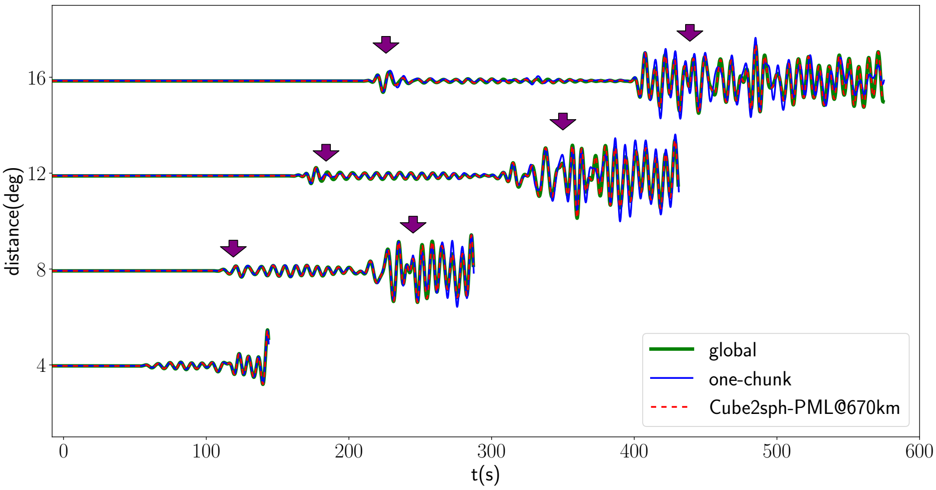

Figure 11: Waveform comparison between simulations using the one-chunk mesh (blue lines) and using the `Cube2sph` mesh truncated at 670 km with PML boundaries (red lines), before surface-wave arrivals. The whole-globe simulation results obtained by AxiSEM (thick green lines) are displayed as background. Purple arrows point to the parts of waveforms where apparent discrepancy can be observed between results of AxiSEM and PML with truncation depth at 220 km (Figure 5b). Truncating the mesh at 670 km while using PML boundaries at the same time enables much more accurate simulation for body waves compared to truncating at 220 km.

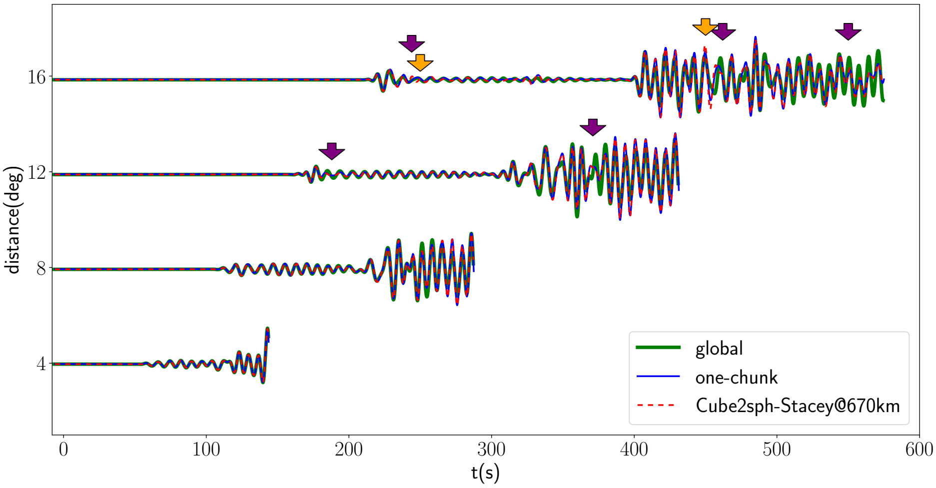

Figure 12: Waveform comparison between simulations using the one-chunk mesh (blue lines) and using the `Cube2sph` mesh truncated at 670 km with the Stacey boundary condition (red lines), before surface-wave arrivals. The full-globe simulation results obtained by AxiSEM (thick green lines) are displayed as background. The results for `Cube2sph` mesh with Stacey condition mostly match well with that of the one-chunk simulation, except for certain time ranges at 16° (orange arrows). With the Stacey boundary condition, the body-wave phases still cannot be accurately simulated even with a larger truncation depth (purple arrows).

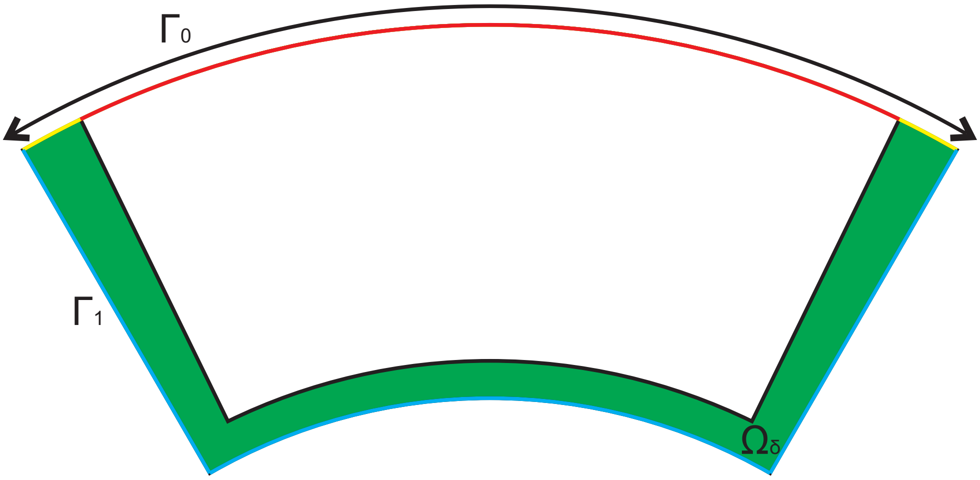

Figure 13: The geometry and notations related to PML. For simplicity, the figure illustrates the 2-D configuration, but can be easily understood in a 3-D setting. The whole computation domain Ω is divided into the PML domain Ω_δ (the green area), and the non-PML domain (the white area). The boundary $\partial\Omega$ contains two parts: the free surface Γ_0 and the outer boundary of the PML domain Γ_1 (the blue line). Furthermore, The free surface Γ_0 has two parts: inside PML $\Gamma_0 \cap \Omega_\delta$ (the yellow line) and outside PML $\Gamma_0 \setminus \Omega_\delta$ (the red line). The boundary $\partial\Omega_\delta$ contains three parts: the outer boundary of the PML domain Γ_1 (the blue line), the inner boundary of the PML domain (the black line) and the part on the free surface (the yellow line).